Cell-Cycle Withdrawal is Graded Rather Than Binary

by

Humza Mohammed Ashraf

B.S., University of Illinois, 2017

A thesis submitted to the

Faculty of the Graduate School of the

University of Colorado in partial fulfillment

of the requirement for the degree of

Doctor of Philosophy

Department of Biochemistry

2023

Committee Members:

Sabrina Spencer

Natalie Ahn

Xuedong Liu

Douglas Seals

Justin Brumbaugh

Ashraf, Mohammed Ashraf (Ph.D., Biochemistry)

Cell-Cycle Withdrawal is Graded Rather than Binary

Thesis directed by Prof. Sabrina Spencer

Chemotherapy treatment elicits a variety of cellular responses such as reversible cell-cycle exit (quiescence) and irreversible arrest (senescence). However, distinguishing between the two is a challenge due to their overlapping molecular markers. To address this issue, we utilized live-cell time-lapse microscopy in this thesis to differentiate reversible from irreversible arrest in cells that are recovering from acute chemotherapeutic stress. We found that heterogeneity in cellular responses can be attributed to p53-p21 signaling, which varies based on the extent of DNA damage. In addition, we developed a new methodology to quantify senescence-associated-beta-galactosidase (SA-β-Gal), a commonly used marker for cellular senescence, and combined it with fluorescent biomarkers of irreversible cell-cycle arrest. By linking numerous senescence biomarkers to previous cell-cycle status, we discovered that the intensities of senescence biomarkers reflect the duration of cell-cycle withdrawal, rather than cellular senescence per se. This suggests that cell-cycle withdrawal is a graded process rather than a binary one, and the intensities of senescence biomarkers can indicate the likelihood of cell-cycle re-entry. Overall, our study suggests that there is no definitive point of no return for cell-cycle re-entry and that the likelihood of re-entry decreases gradually as cells progress through the continuum of cell-cycle exit. Our findings have significant implications for extracting dynamic information from snapshot data, where molecular marker combinations at different intensities encode past temporal histories of single cells and may potentially be used to predict future cell-fate outcomes.

Contents

Chapter

Chapter 1

Introduction

1.1 Cellular proliferation and cell-cycle commitment

The mammalian cell cycle is a highly conserved and ordered process that integrates a multitude of extra- and intra-cellular inputs to drive cellular proliferation [1,2]. Dysregulation of the human cell cycle is a critical hallmark of cancer cells, where chronic cell-cycle progression is sustained even in the absence of normal signal inputs [3,4]. The primary source of these proliferative cues stems from signaling through the mitogen activated protein kinase (MAPK) pathway, which begins with the binding of extra-cellular mitogenic factors, such as epidermal growth factor (EGF), to their cognate growth factor receptors [5]. This binding event causes sequential activation of a series of protein kinases that converges on extracellular-signal-regulated kinase (ERK), which is a critical master regulator of cell fate determination [5,6]. Activation of ERK stimulates the expression of a multitude of transcription factors such as Fos and Jun, which bind to consensus sites on the Cyclin D promoter, giving rise to Cyclin D production [3,6]. Cyclin D protein plays a critical role in driving cell-cycle entry, since it binds and activates cyclin-dependent-kinases 4 and 6 (CDK4/6), which phosphorylate the retinoblastoma protein (Rb), initiating cell-cycle commitment [2,7–10]. However, shortly after CDK4/6 becomes activated, CDK2 takes its place, maintaining the phosphorylation of Rb throughout the remainder of the cell cycle by associating with Cyclin E and Cyclin A [2,11,12]. As a result, CDK2 activity is commonly used to track the cell cycle, since it rises continuously from cell-cycle commitment to division [11,12].

Rb has 14 consensus phosphorylation sites that are strictly either hypo- or hyper-phosphorylated [7,13,14]. In the absence of CDK2 activity, hypo-phosphorylated-Rb binds and inhibits the transcription factor E2F, which is a master regulator of cell-cycle commitment [2]. However, in the presence of CDK2 activity, Rb becomes hyper-phosphorylated, liberating E2F and giving rise

to the simultaneous expression of hundreds of transcriptional targets, committing cells to finishing their current cell cycle [2,12,15]. Inhibition of the MAPK pathway at this point onward does not affect the current cell cycle but rather affects the probability of daughter cells to be born cycling, where CDK2 activity rises shortly after mitosis [12]. However, cells born without hyper-phosphorylated Rb are termed quiescent (G0), where cell-cycle entry is temporarily delayed and instead commences later in the future [12]. For a more detailed description of G0, see Chapter 1.2.

For cells committed to the cell cycle, they must transit through four distinct phases: Gap 1 phase (G1), Synthesis Phase (S), Gap 2 phase (G2), and Mitosis (M). During G1, cells grow in size and prepare their genome for duplication through origin licensing, a process that prevents DNA re-replication [16,17]. During S phase, DNA polymerases make identical copies of all 23 chromosomes to be evenly distributed to each future daughter cell [18]. During G2, cells continue to grow in size, verify the integrity of the genome, and prepare for division [18,19]. Finally, during mitosis, one copy of each sister chromatid is pulled to opposite sides of the cell to give rise to two genetically identical daughters after cytokinesis [20].

Progression through the cell cycle is maintained by the concerted activities of CDK4/6-Cyclin D, CDK2-Cyclin E/A, and CDK1-Cyclin B [2]. These CDKs have a multitude of substrates (the most notable of which is Rb) that play critical roles in maintaining each cell-cycle phase upon phosphorylation [21]. While CDK protein levels fluctuate little throughout the cell cycle, the cyclins are actively synthesized and degraded (by specific E3 ubiquitin ligases) to ensure they are abundant only during specific windows of the cell cycle [22,23]. This ensures that cell-cycle progression is unidirectional, as CDK activity is ordered and sequential.

1.2 Quiescence: the state of reversible cell-cycle withdrawal

While there is extensive literature about the processes that initiate and maintain cell-cycle commitment, withdrawal from the cell cycle remains much more poorly understood. One of the most well-described forms of cell-cycle exit is quiescence, where cells retain their capacity to proliferate and re-enter the cell cycle in the future [24,25]. *In vivo*, quiescence is the default resting

state of many cell types, particularly those implicated in tissue repair, immunity, and reproduction, where exposure to specific stimuli is required for driving cell-cycle re-entry [25]. This ensures that proliferation is tightly controlled and occurs only when needed. *In vitro*, proliferation occurs much more continuously due to the excess of growth factors, nutrients, and low levels of exogenous stress [26–28]. However, in response to mitogen withdrawal, nutrient deprivation, or cellular damage, cells enter a transient state of arrest only to re-enter the cell cycle in the future [29,30].

1.2.1 Stress triggers of quiescent cells

While there are numerous external stresses that can give rise to quiescence, this thesis will only focus on four major ones: serum starvation, MAPK pathway inhibition, contact inhibition, and CDK inhibition [31]. Withdrawal of serum from full growth media in tissue culture or targeted inhibition of proteins in the MAPK pathway (E.g., MEK inhibition) restricts MAPK pathway signaling by limiting ERK activation. This prevents cells from being able to synthesize new Cyclin D, since ERK activation stimulates Cyclin D production, and thus Rb cannot be phosphorylated by CDK4/6 to drive cell-cycle commitment [32]. Similarly, as the local density of cells in culture increases, cell-cell contacts trigger downstream ERK inactivation, pushing cells into a G0 state by limiting Cyclin D synthesis [33]. Finally, CDK inhibition, particularly CDK4/6 inhibition, has recently been shown to push cells into a reversible G0-like state [10]. Unlike other treatments, CDK 4/6 inhibition does not block signaling through the MAPK pathway, but it does prevent the phosphorylation of Rb. Because MAPK activation also stimulates increased cell growth through the PI3K-AKT-mTOR signaling pathway as well as through the p38-MAPK signaling pathway, cells continue to grow in the presence of a CDK4/6 inhibitor [34,35]. This is uncharacteristic of most cells in quiescence, since extensive previous literature has noted that quiescent cells are vastly less metabolic than proliferating cells, and, as a result, they tend to shrink in size when MAPK signaling is inactive [25]. This novel form of quiescence induction is therefore particularly interesting due to the decoupling of cell growth from proliferation.

In addition to cell-extrinsic stresses that induce cells to quiescence, endogenous cell stress can push cells into a spontaneous quiescence, where they are born without hyper-phosphorylated Rb [12,31]. In tissue culture, a majority of cells born into a spontaneous quiescence can be explained by the accumulation of endogenous replication stress as measured by 53BP1 [36], a protein that associates with sites of double-stranded DNA breaks to trigger DNA repair through homologous recombination (HR) or non-homologous end-joining (NHEJ) [37]. The extent of damage is directly correlated with the duration cells spend withdrawn from the cell cycle before re-entering in the future, and the duration of G0 explains a vast majority of the heterogeneity in intermitotic timing (the time from one mitosis to the next) [31,36]. In general, the durations of G1-S-G2-M are much less variable than the duration of G0 among genetically identical single cells in a population, which is a consequence of stress response mechanisms pushing cells into variable G0 durations before cell-cycle re-entry [31].

1.2.2 Endogenous CDK inhibitors and p21 regulation

While quiescence induced by MAPK-pathway inhibition prevents the CDK4/6-mediated phosphorylation of Rb by limiting Cyclin D production, spontaneous quiescence manifests quite differently. In these cells, Cyclin D paradoxically continues to rise as a function of cell-cycle withdrawal time, which has been theorized to be the result of the loss of degradation of the protein during G0, causing it to continue to accumulate from active MAPK signaling [2]. These data beg the question of how spontaneously quiescent cells overcome high levels of Cyclin D to remain in a state of cell-cycle arrest. One explanation for how cells achieve this feat is through the expression of endogenous inhibitors of cell-cycle progression, such as p21 and p27 [11,38,39]. These tumor suppressor proteins bind to the CDK4-Cyclin D and CDK2-Cyclin E complexes and inhibit their ability to phosphorylate Rb. It was recently shown that the ratio between Cyclin D and p27 controls the probability of unperturbed daughter cells to be born cycling versus spontaneously quiescent [33,40]. Thus, the balance between activator and inhibitor signaling may be critical for the induction and maintenance of stress-induced quiescence.

The expression of CDK inhibitors is an essential and universal feature of all forms of quiescence induction [24,25]. While perturbations to mitogenic signaling tend to cause p27 levels to rise, acute DNA damage response signaling promotes p21 production. However, p27 and p21 share a high degree of sequence homology and transcriptional control, so they are thought to have similar functions and regulatory mechanisms [39]. This redundancy is critical, as loss of these tumor suppressor proteins can initiate uncontrolled proliferation and eventually tumorigenesis. Thus, while p21 is the primary tumor suppressor focused on in this thesis, it is important to note that p27 also plays a critical role in blocking cell-cycle progression.

As previously mentioned, p21 is induced in response to DNA damage. Following DNA strand breakages that occur from replication stress or oxidation, 53BP1 is recruited to promote DNA repair while also recruiting p53, one of the most important tumor suppressors in vertebrates [37,39]. While p53 has many roles in stress response signaling, its most common function is to act as a transcription factor for hundreds of target genes, with p21 being among the most notable [41]. Thus, it is unsurprising that p53 is the single most mutated protein in human cancers, since its loss of function allows cell-cycle progression to proceed uninhibited from the lack of p21 induction [41].

Commitment to the cell cycle causes rapid degradation of p21, since CDK2-Cyclin E phosphorylates p21, inactivating it and targeting it for degradation by the proteosome [11]. Thus, p21 inhibits CDK2 activity, which in turn inhibits p21 function, suggesting that cell-cycle commitment depends on the loss of p21. This notion is reinforced by the observation that $p21^{-/-}$ cells fail to undergo spontaneous quiescence, making them more susceptible to damage and apoptosis [11,12]. Thus, p21 plays an essential role in promoting stress-induced cell-cycle withdrawal.

1.3 Senescence: the state of irreversible cell-cycle exit

Senescence is a state of irreversible cell-cycle exit that was originally identified from the observation that primary human cells in culture have limited replicative lifespans due to the “end-

replication-problem", where the ends of linear chromosomes cannot be replicated, leading to chromosome attrition over time [42]. To solve this problem, the ends of chromosomes are capped by repetitive sequences of telomeric DNA (TTAGGG in humans) that are bound to a complex of proteins called shelterin, which shields the exposed chromosome end from initiating DNA break repair [43,44]. However, telomere shortening eventually destabilizes the shelterin complex, exposing chromosome ends and triggering a DNA damage response that pushes cells out of the cell cycle [43,44]. Thus, the cumulative number of population doublings achievable by non-immortalized cells is fixed, tapering off as a function of time. As cells approach this replicative limit, the intermitotic times of single cells in the population become increasingly variable, where some cells continue to cycle rapidly, some cycle slowly, and some never cycle again [45]. The cells that lose their capacity to proliferate altogether are termed senescent and their accumulation is a critical part of tissue aging [46].

1.3.1 Stress triggers of senescent cells and their role in aging and cancer

Senescent cells accumulate in a tissue as a function of time, secreting a wide array of inflammatory cytokines, chemokines, and extracellular proteases that are responsible for initiating a chronic immune response and remodeling the tissue microenvironment [47,48]. This "chronic inflammation" has been termed the senescence-associated-secretory-phenotype (SASP) and creates a permissive environment for tumorigenesis and numerous other disease pathologies [47,48]. The accumulation of senescent cells over time coincides with a sharp decline in stem cell function, where the inability to renew damaged tissue in response to stress promotes tissue deterioration and aging [42]. Furthermore, previous landmark studies found that targeted ablation of senescent cells in mice halted, delayed, and even reversed numerous age-associated pathologies, suggesting that the onset of senescence is a key molecular hallmark of aging [49,50].

In addition to replicative aging, senescence can arise from numerous other external stresses including oncogene overexpression, reactive oxygen species, DNA damaging agents, and targeted cancer therapies [42]. Extensive previous work has clarified that all forms of

senescence induction can be categorized as either p53 or Rb dependent [42,51]. In the former case, a stress response triggered by DNA strand breakages triggers the activation of p53, halting cell-cycle progression through p21 expression. In the latter case, complete inhibition of CDK4/6 activity is sufficient to induce a damage-less and SASP-less senescence, but the precise mechanism of action remains unclear [52].

A growing recent body of literature has emphasized the potential therapeutic benefit of pushing cancer cells into a senescent state [53,54]. While cancer cells normally bypass tumor suppressor mechanisms to maintain uncontrolled proliferation, under the right circumstances, external stress can push these cells out of cycle if the appropriate machinery is intact. For example, p53-competent cancer cells withdraw from the cell cycle when challenged with high doses of chemotherapeutic drugs such as etoposide or doxorubicin [55]. The senescent cells that arise from these therapies not only halt cell-cycle progression but also recruit the innate immune system to the site of the tumor to induce apoptotic cell death. Thus, while senescent cells are deleterious for aging and tissue homeostasis, they play a beneficial role in enhancing the efficacy of cancer therapies through immune cell recruitment [54].

1.3.2 Biomarkers of senescence

While quiescent cells are defined from the fact that they re-enter the cell cycle, senescent cells are much harder to classify, since they are permanently arrested. The most basic feature of senescent cells is that they are not cycling, so they lack proliferation markers [42] such as Ki67 (see Chapter 1.5) and phospho-Rb, and they have elevated levels of tumor suppressor proteins such as p21. However, quiescent cells also share these characteristics, making it unclear whether cells marked as senescent are irreversibly arrested to begin with. Instead, the endogenous CDK4/6-inhibitor p16 is more commonly associated with senescence because it is only expressed in cells permanently withdrawn from the cell cycle [56]. Furthermore, because p16 plays a critical role in halting the proliferation of transformed cells *in vivo*, the genetic locus encoding p16 (CDKN2A) is the most frequently deleted and epigenetically silenced in human cancers [57]. However, there are

numerous drawbacks to using p16 as a standalone marker for senescence: 1) p16 expression levels are low, making it challenging to detect both *in vivo* and *in vitro* [58,59]; 2) p16 but not p53 is dispensable for the induction and maintenance of senescence [51], and 3) p16 is neither directly connected to the DNA damage response (a near universal feature of senescent cells) nor the SASP [51,57]. Thus, in addition to the expression of endogenous CDK inhibitors such as p21 and p16, senescence has been defined by the presence of numerous other molecular markers.

The gold-standard marker of cellular senescence is the senescence-associated-beta-galactosidase stain (SA-β-Gal) [42,60]. β-galactosidase is a lysosomal enzyme that catalyzes the hydrolysis of glycosidic bonds in gangliosides, keratin sulfates, and various glycoproteins. The enzyme attains its highest activity at pH 4.5, yet its activity is read out at a suboptimal pH 6.0, ensuring that signal is detected only when the β-galactosidase protein is highly expressed, a hallmark feature of increased lysosomal content and autophagy [42,61–63]. To measure β-galactosidase activity, fixed and permeabilized samples are fed X-Gal (5-bromo-4-chloro-3-indolyl-beta-D-galacto-pyranoside), an inert colorless substrate that is hydrolyzed by endogenous β-galactosidase to yield 5,5'-dibromo-4,4'-dichloro-indigo-2, an insoluble dark blue product, which can be visualized under a light microscope [64]. A landmark study from 1995 reported that β-galactosidase activity preferentially accumulates in senescent but not quiescent or terminally differentiated cells *in vivo* [60]. As a result, SA-β-Gal staining has become nearly synonymous with stress-induced irreversible cell-cycle withdrawal.

Despite its frequent use, SA-β-Gal staining is challenging to detect and quantify, dispensable for the induction and maintenance of senescence, and not actually specific to only senescent cells [42]. Furthermore, knockout of the gene encoding β-galactosidase (GLB1) does not affect the cell-cycle status of cells pushed into senescence by replicative aging [62]. Thus, β-galactosidase is not required for cells to become senescent. Finally, high basal levels of SA-β-Gal staining are normally observed in phagocytes, Kupffer liver cells, and microglia, calling into

question the markers' "senescence association" [42]. Thus, SA-β-Gal staining is also insufficient as a standalone marker of cellular senescence.

To overcome the limitations associated with p21, p16, and SA-β-Gal staining, several other markers of senescence have been applied with moderate success, including the presence of DNA damage, expression of SASP factors, and aberrant cell size scaling [43,66]. While these markers in isolation are also not unique to senescent cells, their simultaneous presence is a strong indication of irreversible cell-cycle arrest. Since the DNA damage response and the SASP were discussed in detail in sections 1.2.2 and 1.3.1 respectively, only aberrant cell size scaling will be discussed below.

One of the earliest identified features of senescent cells is the fact that they undergo uncontrolled cell growth [66]. Cell growth is defined as the increase in cell size from both biomass accumulation and increased volume; it occurs when the global rate of cellular biosynthesis exceeds the rate of degradation [66,67]. Since a large fraction of cellular macromolecular content consists of protein, ribosome biogenesis and protein synthesis largely dictate the rate of cell growth [68]. During quiescence, proteins associated with cell-cycle progression are not synthesized, causing a reduction in cell size due to reduced macromolecular content [25]. In contrast, senescent cells are extremely metabolically active, as the synthesis and secretion of inflammatory cytokines from the SASP is extremely energetically demanding [69]. However, this continued cell growth phenotype proceeds with imbalanced scaling of the proteome [70]. Normally, the concentration of the cytoplasm is fixed since the volume of the cell increases proportionally to the accumulation of biomass [71]. Nevertheless, recent landmark studies identified that the macromolecular content of cells induced to senescence does not scale with size, causing cytoplasmic dilution and reduced cellular function [70,72,73]. Further investigation of this phenomenon revealed that while many classes of proteins subscale following senescence induction, a subset of the proteome superscales with size, causing many proteins associated with senescence to be highly overrepresented [70,73]. Thus, dysregulated cell growth is now recognized as a hallmark feature of senescent cells.

In addition to the markers addressed above, there are numerous other markers that have also been applied with variable success. These markers include but are not limited to: inflammatory micro-RNAs (E.g., miR-146a) [74], cell-surface proteins for immune cell recruitment (E.g., urokinase-type plasminogen activator receptor (uPAR)) [75], breakdown of the nuclear envelope (E.g., loss of Lamin B1) [76], chromatin remodeling (E.g., loss of HMGB1 and formation of senescence-associated-heterochromatin-foci (SAHF) [77,78]), priming for apoptosis (E.g., CREB and Bax overexpression) [79], altered cellular metabolism (E.g., NAD+/NADH ratio) [69], mitochondrial dysfunction-associated senescence (MiDAS) [80], and reduced autophagic flux (as measured by LC3I/II and activation of mTOR targets) [81]. These markers have proven to be somewhat more context dependent than the primary ones listed earlier, since senescence can manifest differently not only among treatment conditions but also across cell types [82–84].

1.4 Quiescence versus senescence in cancer therapy

Cell-cycle withdrawal prevents damage from being inherited by future daughter cells while also making cells more resilient to further damage [31]. In cancer chemotherapy, slow cycling cancer cells are more resistant to chemotherapy than fast cycling cells because they transit less frequently through S phase and mitosis, the periods of the cell cycle that these therapies target [85,86]. Live-cell imaging of cancer cells released from acute chemotherapy identified that the abundance of p21 protein during the window of drug treatment predicted future cell-cycle commitment outcomes [85]. While the highest and lowest levels of p21 led to senescence, intermediate levels of the protein permitted cell-cycle commitment long after drug washout [85]. As a result, it is theorized that extended chemotherapy treatment eventually selects for a slower cycling subpopulation of cells that can evade the effects of drug, giving rise to tumor relapse [87]. Furthermore, previous work identified that while acute exposure to high levels of ionizing radiation pushes most cells into senescence, a small subpopulation of slow cycling cells always persists due to spontaneous fluctuations in p53 abundance [88]. Thus, the proliferative probability of cells

following acute chemotherapeutic stress is directly tied to tumor suppressor signaling, where the cells that are most likely to cycle have the lowest levels of p53 and p21.

At a snapshot in time, it is unclear which cells withdrawn from the cell cycle following chemotherapy are capable of proliferating in the future versus which will never cycle again. Prognostically, this heterogeneity in fate is detrimental for tumor cell clearance since slow cycling cells are not only more resistant to chemotherapy but also are more prone to mutagenesis, giving rise to recurrence and resistance in the future [87,89]. In contrast, cells permanently exited from the cell cycle cannot initiate population regrowth and thus enhance the efficacy of chemotherapeutic interventions [90]. As a result, a long-term goal in the development of future therapies should be to limit the proportion of cells that enter quiescence by pushing them into senescence instead. However, to do this would require the ability to distinguish quiescent from senescent cells using some combination of novel and existing biomarkers, establishing a unique molecular definition for each cellular state. Such definitions would pave way for the development of new therapeutic approaches that could delay or limit cancer cell relapse and drug resistance.

1.5 Quiescence depth: the gray area between quiescence and senescence

While most literature has favored the use of discrete terminologies to describe cell-cycle exit (E.g., quiescence and senescence), there is a growing body of literature that suggests that withdrawal from the cell cycle is graded rather than binary [91–94]. Cells withdrawn from the cell cycle for extended periods of time by serum starvation have a reduced ability to re-enter the cell cycle following serum re-stimulation, and this phenomenon has been termed quiescence depth [91,92]. As cells move into deeper levels of quiescence, they have a progressively reduced ability to promote the autophagic degradation of damaged cellular material, which in turn gives rise to oxidative species that further promote cellular damage [91]. This cellular damage initiates stress response signaling that activates tumor suppressor signaling, halting cell-cycle commitment. Restoration of autophagic function or scavenging of oxygen free radicals pushes cells into a shallower quiescence, increasing the likelihood for cells to commit to the cell cycle. Thus, quiescence depth

is thought to be regulated by a so-called “lysosomal dimmer switch”, where lysosomal function controls the pE.g.robability for cells to re-enter the cell cycle [91,92].

1.5.1 Comparing deep quiescence and senescence

Transcriptomic analysis of deeply quiescent cells revealed that they highly resemble senescent cells based on their differentially expressed genes [91]. Thus, as cells transit deeper into quiescence, they not only have a reduced ability to re-enter the cell cycle in the future, but they also molecularly become more like senescent cells. These data suggest that quiescence and senescence may not necessarily be distinct cellular states; rather, they may fall on a continuum of cell-cycle withdrawal, where senescence may be a very deep quiescence from which cells are unable to reawaken. Furthermore, this continuum model is supported by several pieces additional of evidence: 1) biomarkers of quiescence and senescence are highly overlapping [42]; 2) long-term quiescent cells transit into senescence in a DNA-damage-dependent fashion [95]; 3) isogenic yeast cells under acute glucose removal become senescent rather than quiescent if they fail to activate Rim-15, a major nutrient-sensing kinase [96]; 4) excessive cytoplasmic dilution of hematopoietic stem cells decreases their function by impairing their ability to exit quiescence with increasing organismal age [97]. Thus, the line separating quiescent from senescent cells is ill-defined, calling into question whether they can be molecularly resolved from each other or whether they are gradations of the same cellular state.

1.6 Studying cell-cycle dynamics using live-cell imaging

Recent advances in time-lapse live-cell imaging have made it possible to track the cell-cycle dynamics of single cells over many days in real time [98,99]. After filming, cells can be fixed and stained for numerous immunofluorescent markers and then the signal in single cells can be mapped back to their live-cell dynamics from the previous several days [2]. This post-hoc analysis provides several unique benefits over classic molecular approaches: 1) the ability to observe cell-cycle-fate-dynamics in real time and thus predict the likelihood of future outcomes 2) the ability to quantify single-cell heterogeneity in both the dynamics and abundance of various markers; 3) and

the ability to multiplex several biomarkers in the same single cells both during and after live-cell imaging. In this thesis, live-cell imaging followed by post-hoc staining was used extensively with two commonly used markers of proliferation: an endogenously tagged mCitrine-Ki67 [94] and a kinase-translocation-reporter (KTR) for CDK2 activity [12].

Ki67 is a commonly used marker of cellular proliferation that rises at the start of S phase and falls immediately after mitosis, and it has prognostic potential for cancer therapeutics [94,100]. The fraction of Ki67 positive cells by immunohistochemistry staining of patient biopsy samples reflects how quickly a tumor is proliferating and can inform clinicians how well a patient is likely to respond to chemotherapy [100,101]. Recently, it was shown that the relative abundance of endogenously tagged mCitrine-Ki67 protein at a snapshot in time encodes temporal information about the timing since the last mitosis up to 40 hours, since the protein levels decay as a function of time [94]. Thus, quantifying the intensity of Ki67 rather than using it as a binary marker provides valuable information about the recent proliferative history of the cell [94].

As stated earlier, CDK2 activity rises continuously throughout the cell cycle from shortly after cell-cycle commitment up until mitosis [12]. As a result, a KTR was developed to read out its activity in real time by fusing a fragment of DNA helicase B (DHB), a substrate of CDK2, to a fluorescent protein (for visualization). As CDK2 activity rises, DHB is phosphorylated at consensus serine residues, masking a strong nuclear localization sequence (NLS) and deprotecting a weak nuclear export sequence (NES). Thus, the relative localization of the sensor can be used to compute the CDK2 activity by taking the ratio of the signal in the cytoplasm to the nucleus. Cells born into the cell cycle are denoted $CDK2^{inc}$ whereas cells born into quiescence are denoted $CDK2^{low}$ [12].

1.6.1 Overview of distinguishing quiescence and senescence

Because quiescence and senescence can be triggered by similar stressors and share common biomarkers, it is unclear whether they are distinct biological states. The ability to separate these two phenotypes would be beneficial for understanding mechanisms of tumor

relapse, establishing a more universal definition for senescent cells, and uncovering novel mechanisms of cell-cycle control upon re-entry from an arrested state. To address this question, the work in this thesis applies long-term live-cell timelapse imaging followed by immunofluorescence staining to 1) establish cell-cycle based definitions for quiescence and senescence following external cell stress, and 2) quantitatively compare the ability of senescence biomarkers to resolve “truly senescent cells” within a heterogenous population. These studies revealed that cell-cycle withdrawal is graded rather than binary, where the duration of cell-cycle exit following external cell stress is integrated by the intensities of canonical senescence biomarkers in both quiescent and senescent cells alike. The implications of these findings are expanded on in greater detail in the discussion chapter.

Chapter 2

Exposure to acute chemotherapeutic stress induces a gradient of cell-cycle outcomes

2.1 Abstract

Cells withdraw from the cell-cycle in a DNA-damage-response dependent fashion to avoid giving rise to aberrant daughters after chemotherapy treatment. While some cells enter a transient state of arrest (quiescence) and resume proliferation in the future, others exit the cell-cycle permanently to become senescent. Here, we used live cell timelapse microscopy to film single-cells recovering from acute genotoxic stress and separated reversibly arrested cells from irreversibly arrested cells. Furthermore, we linked this phenotype to the extent of DNA damage by staining for 53BP1, which we showed activates the p53-p21 tumor suppression pathway. These data show that senescence is induced incompletely in culture, and this heterogeneity is a direct consequence of differences in the extent of tumor suppressor signaling.

2.2 Introduction

Classically, quiescence is defined by the cell-cycle withdrawal phenotype that emerges from transient inhibition of either the MAPK or Rb pathways[25]. Release from these perturbations allows cells to re-enter the cell cycle through either the accumulation of proliferative drivers such as Cyclin D or through the degradation of tumor suppressors such as p21 and p27[33,40]. However, recent work has shown that quiescence also emerges under conditions of acute, endogenous stress (E.g., replication stress and DNA damage) both *in vitro* and *in vivo*[36,102–104]. In these cases, stress response machinery such as ataxia telangiectasia and Rad3-related protein (ATR) and ataxia-telangiectasia mutated (ATM) can initiate exit from the cell cycle through downstream activation of p53, which transcriptionally controls p21, an inhibitor of several CDK-Cyclin complexes that are responsible for the phosphorylation of Rb[36,103,104]. Several studies have identified that the duration that cells spend in a transient state of arrest is a direct function of the level of damage that initially triggered the stress response[104]. As a result, spontaneous

heterogeneity in the rate that single cells in a population cycle is a direct consequence of differences in the extent of endogenous stress.

Withdrawal from the cell cycle can also be induced through exposure to high levels of DNA damaging agents such as etoposide or doxorubicin, which are commonly used anti-cancer chemotherapeutic agents that inhibit topoisomerases to induce DNA damage and push cells into senescence[85,88,105]. In these cases, the cell-cycle exit phenotype that emerges is thought to be permanent, since the extent of damage is so high that it becomes virtually irreparable. However, lineage analysis of individual cells within these populations has recently revealed substantial heterogeneity in the efficiency of senescence induction. Specifically, some cells evade senescence by entering quiescence[85]. These cells are protected from the accumulation of DNA damage that would subsequently occur in S-phase, the time at which cells are most prone to genotoxicity[86].

To exemplify this, Hsu et al., 2019 utilized single-cell time-lapse imaging and cell tracking to follow cellular behavior during a 24h doxorubicin treatment and for the subsequent 3 days after drug washout[85]. The authors analyzed the movies to find that the initial p21 dynamics during the 24h drug treatment predict the senescent versus proliferative fate of individual cancer cells 4 days later. Cells that were in S/G2 at the time of doxorubicin treatment had low levels of p21 (due to ongoing degradation of p21 by E3 ligases in S phase), accrued more DNA damage than G0/G1 cells, and adopted a senescent fate. By contrast, cells that were in G0/G1 during the treatment window rapidly upregulated p21, had lower levels of DNA damage, and later went on to divide, which correlated with a return to baseline p21 levels. Consistent with this, Ryl et al., 2017 identified that rapidly proliferating Myc-driven cancers can enter a transient, p21-dependent G0 state when challenged with doxorubicin only to re-enter the cell cycle following drug washout[105]. Furthermore, the cells that go on to nucleate colonies in the future have upregulated DNA repair during the drug-treatment window, explaining how a subset of cells is capable of fully rebounding from acute exposure to drug.

In addition to senescence evasion, it has previously been reported that some cells can escape from senescence to re-enter the cell cycle in the future [106,107], implying that senescence is not truly irreversible to begin with. Such claims stem from the fact that following senescence induction *in vitro*, the population gradually regrows over time, implying that cells re-enter the cell cycle from an arrested state. However, it has never been shown that these cells were truly senescent to begin with, as they may be quiescent cells that retained their proliferative capacity all along. Thus, assuming senescence is truly irreversible, there are two primary subpopulations from which regrowth from acute genotoxic stress could occur: 1) cells that evade the DNA damaging effects of therapy (because they were not in S phase at the time of treatment) or 2) cells that incur DNA damage, exit the cell cycle, and later re-enter the cell-cycle from quiescence [108,109]. The latter case implies that some proportion of non-cycling cells at a snapshot in time after chemotherapy treatment may be quiescent rather than senescent. These fates are challenging to distinguish without temporally precise tools and thus pose a serious concern for the efficacy of chemotherapeutic interventions *in vivo*. While senescent cells promote tumor clearance through recruitment of the innate immune system, quiescent cells become less sensitive to repeated rounds of drug treatment, initiating tumor cell regrowth through cell-cycle re-entry in the future[110–112].

To distinguish these outcomes, a recent study by Reyes et al., 2018 tracked single cell fates after increasing doses of ionizing radiation, a commonly used method to induce DNA damage, cell death, and senescence in cancer cells[109]. At even the highest level of damage (20 Gy), there was a subpopulation of cells that was able to exit long-term arrest and re-enter the cell cycle. Multiplexing markers of cell-cycle commitment with fluorescently tagged p53 or 53BP1 revealed that fluctuations in the amplitude of p53 oscillations but not the extent of DNA damaged correlated with the timing of cell-cycle re-entry. Thus, signaling through the p53-p21 pathway is a critical determinant of cell-cycle fate outcomes following acute chemotherapeutic stress.

To reconcile these recent findings, we sought to more broadly quantify the proportion of population regrowth that stems from quiescent cell-cycle re-entry. Additionally, we tested whether this re-entry phenotype was dependent upon a DNA damage response as well as p21 abundance.

2.3 Results

2.3.1 A subset of cells re-enters the cell cycle from quiescence and contributes to population regrowth following chemotherapy treatment

To measure the heterogeneity in cell-cycle fates following senescence induction (**Fig. 2.1A**), we treated MCF10A non-transformed mammary epithelial cells with etoposide, a commonly used anti-cancer chemotherapeutic agent that inhibits topoisomerases to induce DNA damage and senescence[113]. MCF10A cells were released for 1-9d from a 24h treatment of 10 μM etoposide, and cells were fixed and stained for the proliferation marker Ki67 (**Fig. 2.1B and Fig. 2.1C**). Over the duration of recovery from drug, the majority of cells initially withdrew from the cell cycle, but the population began to rebound starting at day 6. This proliferation rebound was confirmed in MCF10A cells with an alternative proliferation marker (Rb phosphorylation, a cell-cycle marker that turns on when cells commit to the cell cycle and turns off when cells exit the cell cycle)[28], as well as in RPE-hTERT, MCF7, and WI38-hTERT cells (**Fig. 2.2A-C**). To ensure our phospho-Rb-high cells were classified accurately, we showed that the same cells were called phospho-Rb-high with or without normalization to total-Rb (**Fig. 2.2D**). Furthermore, while we observed further decreases in the proportion of proliferating cells at increasing doses of etoposide, but there was no concentration of drug (up to 50 μM) that eliminated all cycling cells to yield a pure senescent population (**Fig. 2.2E**).

The proliferating cells rapidly overtake the non-cycling cells by day 9 after chemotherapy treatment, but it remains unclear what proportion of the non-cycling cells at a snapshot in time are quiescent rather than senescent. To address this question, we used MCF10A cells in which Ki67 was tagged at the endogenous locus with mCitrine[114] to isolate non-cycling Ki67^{off} cells by flow cytometry 5d after treatment with etoposide, as this was the time point with the fewest cycling

cells (**Fig. 2.1B**). The levels of Ki67 protein decays with second order kinetics upon cell-cycle exit, hitting the floor of detection after 40h[114]. Thus, Ki67^{off} cells at the time of sorting have been out of the cell-cycle (quiescent or senescent) for at least 40h. Immediately after sorting, we replated the Ki67^{off} cells and began filming them the following day for an additional four days. 100% of the untreated, rare spontaneously quiescent Ki67^{off} cells re-entered the cell cycle within the first two days of filming, consistent with their quiescent status at the time of sorting. Surprisingly, despite the strong senescence-inducing conditions, 28% of etoposide-released cells resumed proliferation at some point during live-cell imaging (**Fig. 2.1E**). Similar results were obtained when this experiment was repeated with 10 Gy ionizing radiation (**Fig. 2.2E**). Thus, a significant fraction of non-cycling cells 5d after chemotherapy or ionizing-radiation treatment are actually quiescent and not senescent, since they are fated to re-enter the cell cycle in the future.

This heterogeneity in cell-cycle fates is also problematic for bulk 'omics studies of senescence, since these studies typically proceed with measurements several days after senescence induction without any isolation of non-cycling cells. To estimate the amount of signal that may come from non-senescent cells in this type of experiment, we noted that 89% (**Fig. 2.1E**) of the original 83% of Ki67^{off} cells (**Fig. 2.1B, 5d timepoint**) remained persistently non-cycling throughout the subsequent four days of filming. Thus, we calculate that about a quarter of cells $(1 - (0.89 \times 0.83))$ would have been misidentified as senescent at 5d after etoposide release.

2.3.2 The extent of DNA damage explains heterogeneity in cell-cycle fate in etoposide-released cells

Because genotoxic stress drives senescence induction[115], we tested whether the rebound in proliferation is coupled to the repair of DNA damage during recovery from etoposide by measuring both Rb phosphorylation and 53BP1, a protein that forms large nuclear bodies at sites of DNA damage[116]. Over the course of recovery from etoposide release, DNA-damaged 53BP1+ cells were persistently high in both the cycling-pRb^{high} and the non-cycling-pRb^{low} fractions (**Fig. 2.3A**). Thus, the presence or absence of 53BP1 nuclear bodies alone is not singularly coupled

to the regrowth phenotype, consistent with previous observations that the presence of damage does not prohibit cell cycle re-entry[109] . However, when we grouped the fraction of cycling and non-cycling cells by the number of 53BP1 nuclear bodies, we found that cells with the highest level of damage were almost uniformly associated with the pRb^{low} state (**Fig. 2.3A**)**.** Thus, the extent of DNA damage explains the heterogeneity in cell-cycle fate following etoposide release. This result was further supported by the fact that the fraction of cycling cells within the population released from 10 μM etoposide decreased exponentially with respect to the number of 53BP1 puncta (**Fig. 2.3B and Fig. 2.3D**), and the size of cells followed the inverse relationship, which is consistent with the loss of cell-size control and proteome scaling imbalance in senescent cells (**Fig. 2.3C and Fig. 2.3D**).

Furthermore, when we performed a similar experiment with cells recovering from 10 Gy of ionizing radiation (**data not shown**), we did not observe the same DNA-damage phenotype, reinforcing the observation from Reyes et al., 2018 that the extent of damage does not prohibit re-entry to the cell-cycle following irradiation[88]. Without elevated damage to reinforce arrest, p53 abundance periodically fluctuates following irradiation stress, causing a subset of cells to spontaneously re-enter the cell cycle.

2.3.3 p53 activates p21, which scales with the extent of DNA damage and reinforces arrest via the Rb pathway following etoposide release

Since the fraction of non-cycling cells scales with increasing levels of damage (**Fig. 2.4**), we next questioned whether the abundance of p21 was also directly correlated with 53BP1 foci. To test this, we treated cells with increasing concentrations of etoposide and quantified p21 and 53BP1 and identified a dose-dependent response for both markers (**Fig. 2.5**). Furthermore, we selected the 10 μM dose and binned cells at increasing numbers of 53BP1 puncta and quantified the average p21 intensity for each bin. As expected, we found that the level of damage was directly tied to the abundance of p21 protein, supporting the notion that heterogeneity in cell-cycle fate following senescence induction is a consequence of variability in p21 signal (**Fig. 2.6**).

Additionally, we compared the levels of p53 and p21 in single cells after etoposide release and found that they were linearly correlated, suggesting that increased damage stabilizes p53, which in turn promotes the activation of p21 (**Fig. 2.7**). Finally, we quantified the ratio of Cyclin D to p21 at increasing doses of etoposide due to recent reports that the relative abundance of activator-to-inhibitor signaling dictates cell-cycle outcomes following acute stress. As expected, the ratio of Cyclin D to p21 fell at increasing doses of etoposide, suggesting that the dose-dependent switch from reversible to irreversible arrest is governed by the abundance of both pro-proliferative and anti-proliferative signals (**Fig. 2.8**).

2.4 Discussion

Previous studies have reported that in certain contexts cells can escape from senescence to resume proliferation in the future[106,117]; however, our time-resolved analysis of single-cells induced to senescence suggests that this regrowth phenotype stems from cells that were never truly senescent. Instead, quiescent cells that retain their capacity to proliferate can outcompete true senescent cells over time in a heterogenous population. Furthermore, the proportion of non-cycling cells rises as a function of etoposide concentration, suggesting that the probability for cells to be truly senescent depends on the extent of DNA damage. While these data are inconsistent with previous observations from Reyes et al., 2018, we suggest that this is due to the fact that irradiation stress is much more transient than etoposide treatment[109]. Despite this, we, Reyes et al., 2018, and Hsu et al., 2019 all found that the p53-p21 signaling pathway dictates the proliferative probability of cells induced to senescence[108,109]. These results indicate that loss of Rb-pathway inhibition drives cell-cycle re-entry, but the cause of this specific loss appears to be context dependent. While the extent of damage is well-correlated with the proliferative probability in our case, it remains to be seen whether it is both necessary and sufficient for cells to be senescent. Future studies able to decouple the presence of damage from proliferative arrest will help to elucidate the precise mechanism by which cells are able to withdraw permanently from the cell-cycle following acute chemotherapeutic stress.

2.5 Materials and Methods

2.5.1 Antibodies and reagents

Anti-Ki67 (ab15580) was purchased from Abcam and used at a 1:2000 dilution. pRb (S807/811) D20B12 XP (8516) was purchased from CST and used at a 1:500 dilution. Anti-human 53BP1 (612523) was purchased from BD and was used at a 1:1000 dilution. Alexa fluor secondary antibodies (A10521, A10520, A-21236, and A-21245) were all purchased from Thermo Scientific and used at 1:1000 dilutions. Hoechst 33342 was purchased from Thermo Scientific (H3570) and used at a 1:10,1000 dilution. Etoposide (E1383) was purchased from Sigma.

2.5.2 Cell lines and culture media

MCF10A (ATCC CRL-10317) cells were obtained from ATCC and grown in DMEM/F12 supplemented with 5% horse serum, 20 ng/ml EGF, 10 µg/ml insulin, 0.5 µg/ml hydrocortisone, 100 ng/ml cholera toxin, and 100 µg/mL of penicillin and streptomycin. During live-cell imaging, phenol red-free full growth media was used. RPE-hTERT (ATCC CRL-4000) were obtained from ATCC grown in DMEM/F12 supplemented with 10% FBS, 1x Glutamax, and 100 µg/mL of penicillin and streptomycin. MCF7 (ATCC HTB-22) were obtained from ATCC and grown in RPMI supplemented with 10% FBS, 1x Glutamax, and 100 µg/mL of penicillin and streptomycin. WI38-hTERT cells were grown in DMEM supplemented with 10% FBS and 100 µg/mL of penicillin and streptomycin. All cell lines were grown in a humidified incubator at 5% CO2 and 37 °C.

2.5.3 Drug treatments

MCF10A cells were plated at 100,000 cells per well in a plastic 6 well culture plate before being treated with 10 µM etoposide the following day for 24h. Etoposide was removed and cells were washed once with PBS before being returned to full growth media. The cells were maintained in culture throughout the duration of drug recovery with media refreshes every 3d. 24h prior to imaging, the etoposide-released cells were trypsinized and replated onto a collagen coated (1:50 dilution in water) (Advanced BioMatrix, No. 5005) 96-well glass-bottom plate (Cellvis

Cat. No. P96-1.5H-N) at 1500 cells per well for live-cell imaging and 3000 cells per well for immunofluorescence.

2.5.4 Flow cytometry

MCF10A cells endogenously tagged with mCitrine-Ki67 and expressing H2B-mTurquoise and DHB-mCherry were trypsinized and resuspended in PBS + 1% FBS + 100 µg/mL of penicillin and streptomycin after a 5d recovery from a 24h treatment with 10 µM etoposide or 10 Gy of ionizing radiation. Unlabeled wild-type cells were used to gate $Ki67^{off}$ cells, which resulted in 25% of etoposide treated cells and 10% of IR treated cells being sorted and replated directly onto a collagen coated (1:50 dilution in water) (Advanced BioMatrix, No. 5005) 96-well glass-bottom plate (Cellvis Cat. No. P96-1.5H-N) for live-cell imaging that started the following day. As a control, the bottom 7.7% of untreated cells were also sorted and plated.

2.5.5 Immunofluorescence

MCF10A cells were treated with 10 µM etoposide for 24h, washed, and allowed to recover before being seeded onto a collagen coated (1:50 dilution in water) (Advanced BioMatrix, No. 5005) 96-well glass-bottom plate (Cellvis Cat. No. P96-1.5H-N) 24h prior to fixation for 15 minutes with 4% PFA in PBS. Cells were permeabilized at room temperature with 0.1% TritonX for 15 minutes and blocked with 3% Bovine Serum Albumin (BSA) for 1h. Primary antibodies were incubated overnight in 3% BSA at 4 °C and secondary antibodies were incubated for 1-2h in 3% BSA at room temperature. Nuclei were labelled with Hoechst at 1:10,000 in PBS at room temperature for 15 min. Two 100 uL per well PBS washes were performed between each described step. All images were obtained using a 10x 0.4 numerical aperture objective on a Nikon TiE microscope.

2.5.6 Time-lapse microscopy

MCF10a cells were plated 24h prior to imaging and full growth media was replaced with phenol red-free full-growth media. Images were taken in CFP, YFP, and mCherry every 12 minutes at two sites per well that were spaced 2 mm apart. Total light exposure was kept below

600 ms. Cells were imaged in a humidified, 37°C chamber at 5% CO2. All images were obtained using a 10x 0.4 numerical aperture objective on a Nikon TiE microscope.

2.5.7 Image processing

Image processing and cell tracking were performed as previously described[118]. Phosho-Rb was separated into high and low modes by using the saddle-point in the data as the cutoff. Ki67^{off} cells were classified as those less than the 95th percentile of the median nuclear signal in WT cells. Quantification of 53BP1 puncta was determined using a previously described approach [116]. Nuclear signals were quantified from a nuclear mask, which was generated using Otsu's method on cells stained for Hoechst. The regionprops function in MATLAB was used to quantify the mean signal for each stain from binary masks of the nucleus.

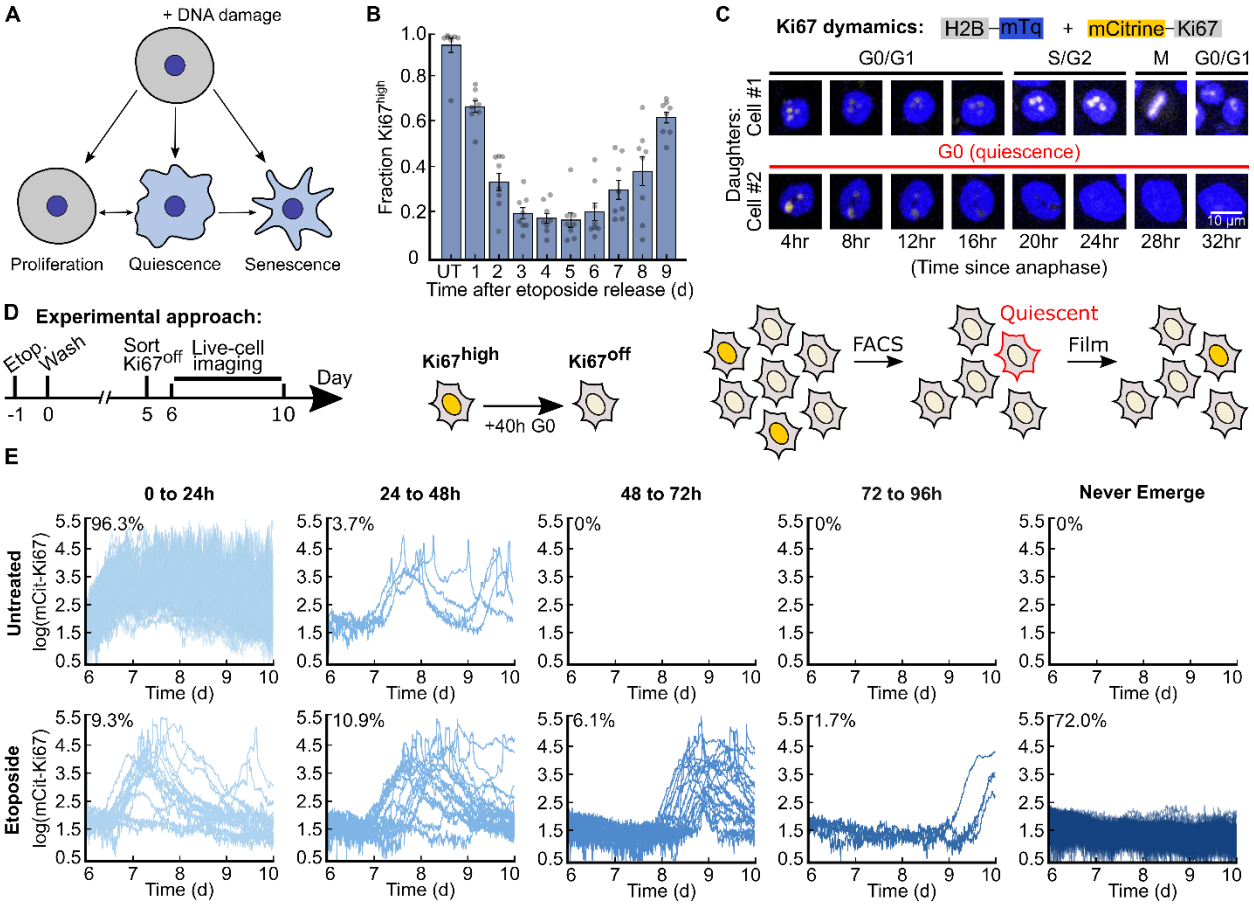

Figure 2.1 A subpopulation of cells exits quiescence to re-enter the cell cycle after DNA damage stress (A) Multiple cell fates arise during recovery from acute DNA damaging agents. (B) MCF10A cells were treated with 10 μM etoposide for 24h before being washed and allowed to recover for 1 to 9d. Cells were fixed and stained for Ki67, and the fraction of Ki67^{off} cells was calculated for each condition. (C) Dynamics of mCitrine-Ki67 with respect to cell cycle phase in 2 daughter cells originating from the same mother. (D) Experimental schematic: MCF10A cells expressing endogenously tagged with mCitrine-Ki67 were plated on day 0 and treated on day 1 with 10 μM etoposide for 24h and washed. On day 5, Ki67^{off} cells were isolated by flow cytometry, plated, and allowed to grow for 24h before being imaged for 96h by time-lapse microscopy. (E) Single-cell traces are grouped based on their relative timing of cell-cycle re-entry from the Ki67^{off} state and the percent of cells in each group is indicated. 200 cell traces total are plotted in each row.

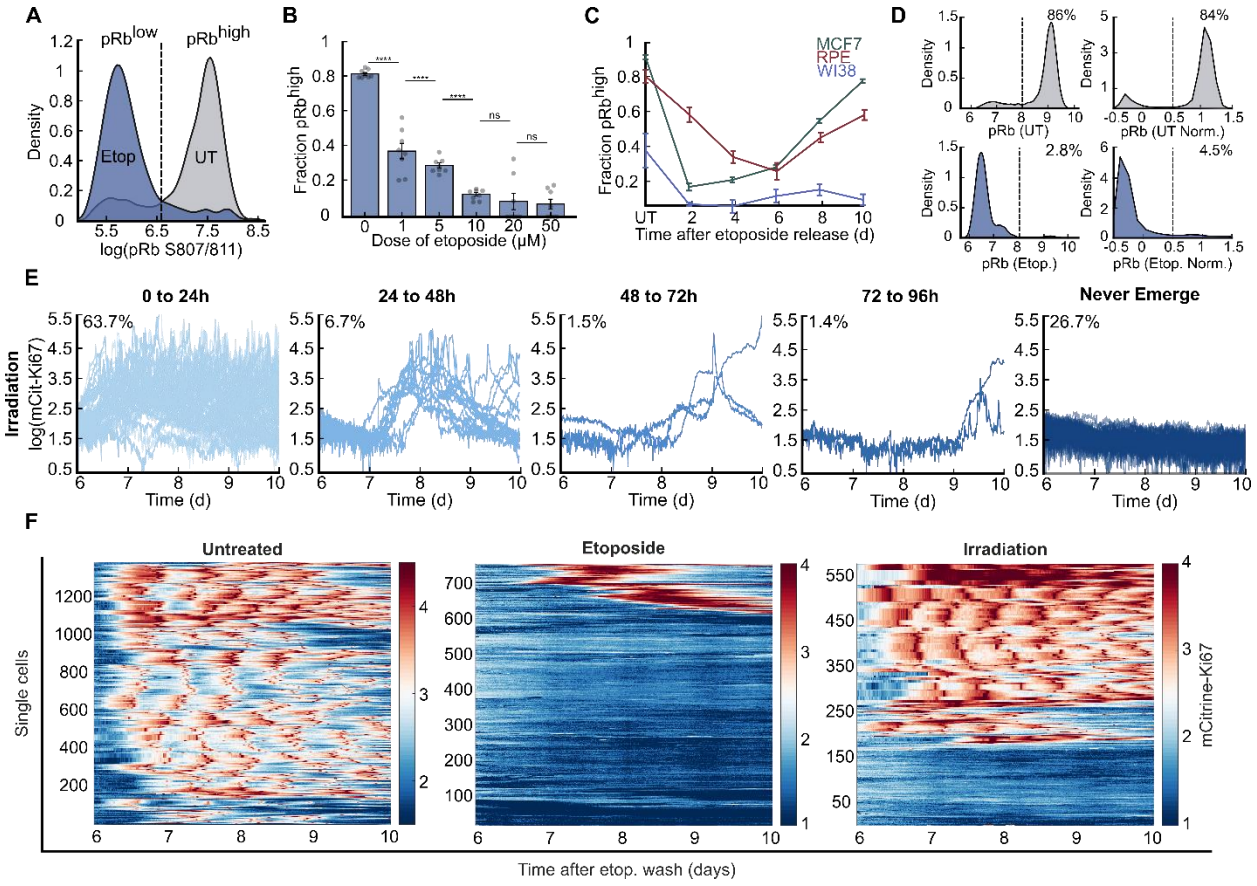

Figure 2.2 Release from acute DNA damage stress universally induces population heterogeneity in cell cycle fate (A) (A) Definition of phospho-Rb^{low} versus phospho-Rb^{high} in MCF10A cells released from a 24h treatment of 10 μM etoposide for 6d. (B) MCF10A cells were treated with increasing concentrations of etoposide for 24h before being fixed and stained for phospho-Rb at 6d after release from drug. (C) MCF7, RPE-hTERT, and WI38-hTERT cells were treated with 10 μM etoposide for 24h before being washed and allowed to recover for up to 10d. (D) Fraction of cells classified as phospho-Rb^{high} before and after normalization to total Rb (E) MCF10A cells expressing endogenously tagged mCitrine-Ki67 were plated on day 0 and treated with 10 Gy ionizing radiation the following day. On day 5, Ki67^{off} cells were isolated by flow cytometry, plated, and allowed to grow for 24h before being imaged for 96h by time-lapse microscopy. Single-cell traces are grouped based on their relative timing of cell-cycle re-entry from the Ki67^{off} state and the percentage of cells in each group is indicated. 200 traces are plotted in total. (F) Heatmaps of all traces from time-lapse microscopy for untreated, etoposide-released, and irradiated cells from Fig. 1.1E and Fig. 1.2E.

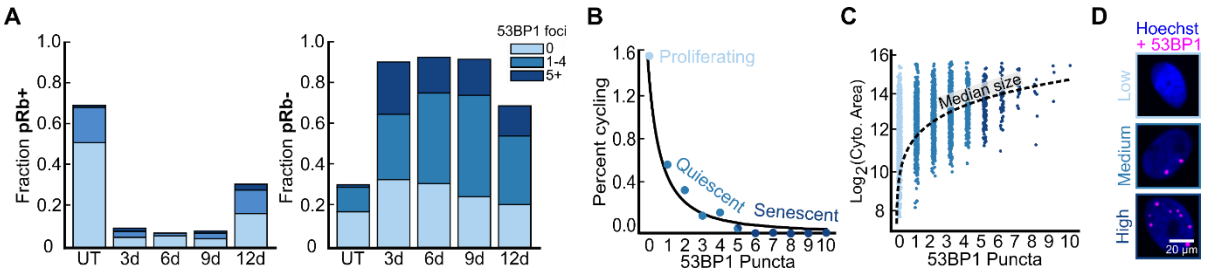

Figure 2.3 The extent of DNA damage after etoposide release dictates cell-cycle fate (A) 53BP1 nuclear body detection by immunofluorescence after recovery from a 24 hr treatment of 10 μM etoposide in pRb^{high} versus pRb^{low} MCF10A cells. (B) The percentage of pRb^{high} cells at different levels of 53BP1 accumulation 6d after treatment of MCF10A cells with 10 μM etoposide for 24 hr. (C) Cytoplasmic area (as measured by succinimidyl ester staining) was compared against the number of 53BP1 nuclear foci from the the same cells in Fig. 2.3B. (D) Representative cells stained with Hoechst and 53BP1 at different levels of damage following etoposide release.

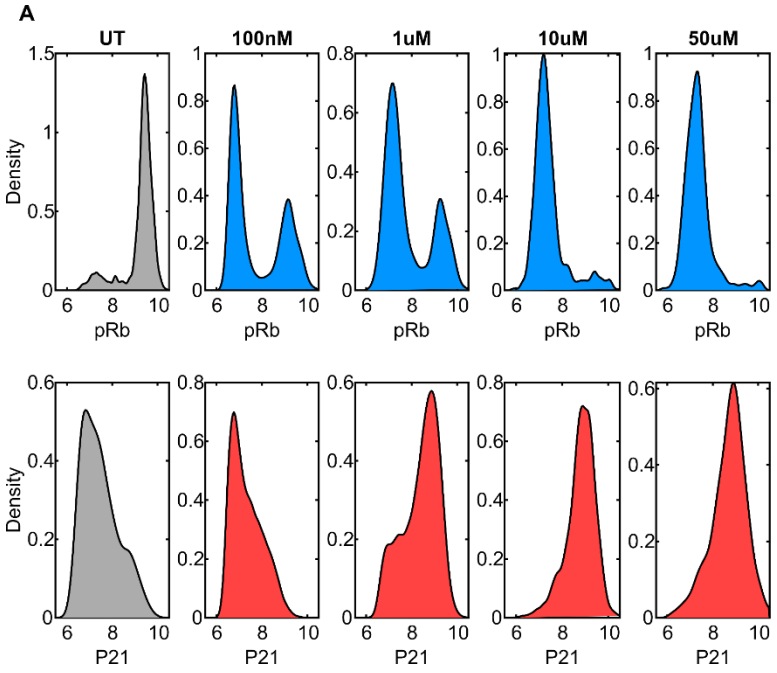

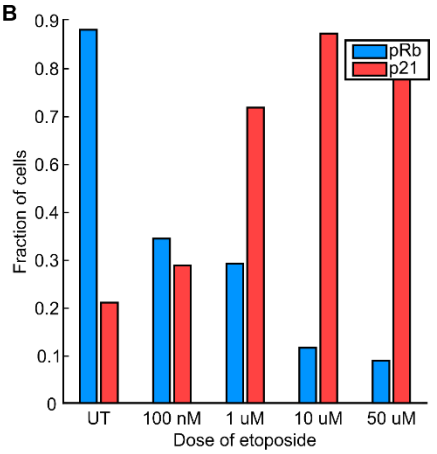

Figure 2.4 Etoposide dose response (A) pRb and p21 staining after a 24 hr treatment of 10 μM etoposide followed by 6d recovery in MCF10A cells. (B) The fraction of pRb^{high} and p21^{high} from Fig. 2.4A.

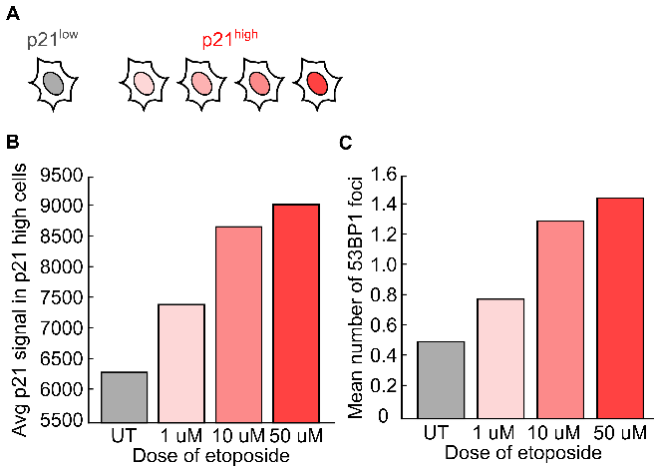

Figure 2.5 p21 scales with damage, and its intensity is graded rather than binary after release from etoposide (A) Schematic of gradation in p21 signal after a 24 hr treatment with etoposide followed by 6d recovery. (B) Mean p21 signal within the p21^{high} cells at increasing doses of etoposide. (C) Mean number of 53BP1 foci at increasing doses of etoposide.

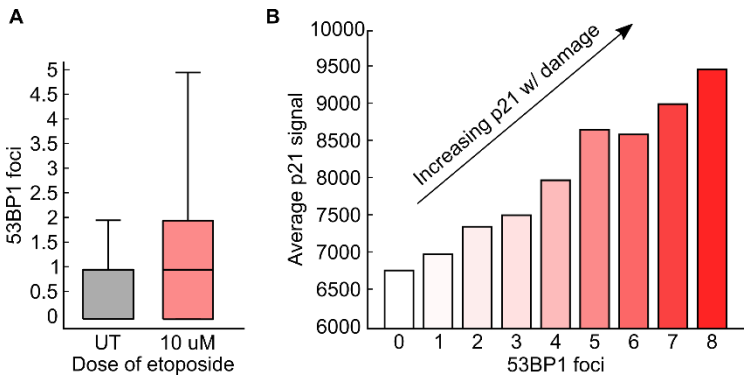

Figure 2.6 p21 intensity scales with the extent of DNA damage (A) Distributions of 53BP1 foci number after a 24 hr treatment of 10 μM etoposide followed by 6d recovery in MCF10A cells. (B) The mean p21 signal as a function of 53BP1 foci number in cells released from of 10 μM etoposide.

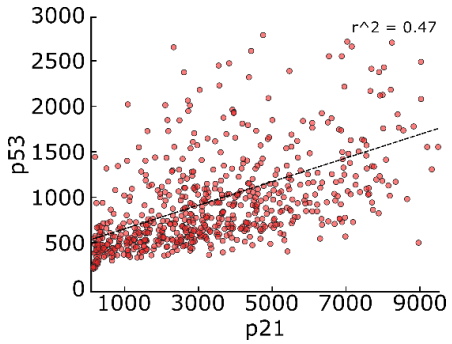

Figure 2.7 p53 and p21 are correlated after release from etoposide Cells were co-stained for p53 and p21 after a 24 hr treatment of 10 μM etoposide followed by 6d recovery in MCF10A cells.

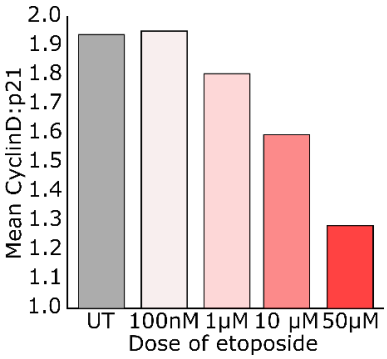

Figure 2.8 CyclinD:p21 falls at increasing doses of etoposide Cells were co-stained for Cyclin D1 and p21 and the ratio of their means was taken at increasing doses of drug (24 hr treatment) followed by 6d recovery in MCF10A cells.

Chapter 3

SA-β-Gal staining is a graded marker of cell-cycle exit duration rather than senescence

3.1 Abstract

The gold-standard method for detecting senescent cells is the senescence-associated-beta-galactosidase (SA-β-Gal) stain. However, this marker is non-binary, often used qualitatively and subjectively, and may not be specific to senescence, making it unclear how to interpret heterogeneous levels of the SA-β-Gal stain across a population of single cells. Here, we filmed single cells recovering from acute genotoxic stress and compared their relative SA-β-Gal signals at the end of the movie using a novel approach for quantifying this colorimetric stain. These data revealed that increased duration of cell-cycle exit is directly corelated with the intensity of SA-β-Gal staining and is present in slow-cycling, quiescent, and bona fide senescent cells. Finally, we confirmed that increased SA-β-Gal staining scales with increased lysosomal mass and autophagy with single-cell resolution.

3.2 Introduction

The gold-standard marker for detecting senescent cells is the senescence-associated-beta-galactosidase (SA-β-Gal) stain[119,120]; however, the β-galactosidase gene is dispensable for the induction and maintenance of senescence[121], raising questions about a causal relationship between SA-β-Gal positivity and irreversible cell-cycle withdrawal. One landmark study to address what SA-β-Gal may be readout for was Kurz et al., 2000, which focused on the lysosomal localization of the enzyme[61]. The authors first identified that both SA-β-Gal staining and lysosomal content (as measured by acridine orange) increased as a function of passage number in replicative senescence, suggesting that SA-β-Gal may be correlated with increased lysosomal mass in senescent cells. Consistent with this, the levels of SA-β-Gal protein increased as a function of cell passage number, indicating that the abundance of lysosomal proteins may scale with lysosomal content under conditions of stress. Furthermore, the authors found that SA-β-Gal staining is sensitive to lysosomal de-acidification in live cells by treatment with bafilomycin, a

vacuolar H^+-ATPase inhibitor, suggesting that lysosomal function may also be an important determinant of SA-β-Gal positivity. Previous studies have suggested that senescent cells have reduced autophagic efficiency, which may be a consequence of a discrepancy in lysosomal mass and lysosomal function; however, this has never been directly shown with quantitative resolution in single cells due to an inability to quantify the SA-β-Gal stain and multiplex it with other markers. In fact, most studies simply binarize the colorimetric stain by manually labelling cells either blue (senescent) or not blue (not senescent)[119,121]. However, closer inspection of these images reveals substantial heterogeneity in the extent of staining among single cells in the population, with no obvious threshold for designating a cell positive for SA-β-Gal. Furthermore, because the stain has rarely been overlaid in single cells with orthogonal markers, it is unclear how SA-β-Gal positivity *directly* relates to other features of senescence. As a result, there is a critical need to develop a robust method for quantifying SA-β-Gal staining and combining it with other markers to more thoroughly examine its relationship to irreversible cell-cycle arrest and changes in autophagy.

3.3 Results

3.3.1 A novel method for quantifying SA-β-Gal staining

To address the critical need in the senescence field for quantification of the SA-β-Gal stain, we adapted an existing method[118] to develop an automated the SA-β-Gal stain is primarily composed of blue and green pigments that preferentially absorb red light. Thus, the SA-β-Gal stain can be most easily quantified as the absence of red signal within every cell, and this channel has the largest dynamic range relative to background (**Fig. 3.1A**). We used the value at the 5^{th} percentile of red pixels within the cytoplasm of each cell as the SA-β-Gal score, since this method visually matched the relative blueness of cells (**Fig. 3.1B**) and recapitulated the gradient of staining in single cells induced to senescence (**Fig. 3.2**). To validate the SA-β-Gal quantification method, the upper and lower quartiles of SA-β-Gal intensities were displayed through a binary cytoplasmic mask filter that was gated from the distribution of SA-β-Gal values after a 4d release from a 24h pulse 10 μM etoposide (**Fig. 3.3A**). Despite the fact that SA-β-Gal is almost always

used as binary marker of senescence, we found that the distribution of the SA-β-Gal signal is graded rather than binary, with no clear cut-off for designating a cell as senescent (**Fig. 3.1B**).

Furthermore, SA-β-Gal staining intensity is sensitive to the cell fixation method; 2% PFA and SA-β-Gal CST kit fixatives were compared (**Fig. 3.2C**). Although the dynamic range of SA-β-Gal staining is larger for the kit fixative compared to 2% PFA, the kit fixative is less compatible with subsequent immunofluorescence staining (excluding LAMP1) (**Fig. 3.2B**). The kit fixative was used for SA-β-Gal staining following all live-cell imaging experiments and LAMP1 immunofluorescence. 2% PFA was used for all other SA-β-Gal + immunofluorescence experiments. Additionally, immunofluorescence co-staining with SA-β-Gal is limited to the Cy5 channel due to strong bleed-through fluorescence in the GFP channel and partial bleed-through into the Cy3 channel after staining with SA-β-Gal (kit fixative) (**Fig. 3.2C**).

3.3.2 SA-β-Gal staining overlaps between quiescent and senescent cell fates

Applying our new method, we co-stained cells with SA-β-Gal and an antibody against Rb phosphorylation, a marker of cell cycle commitment[122], and discovered a surprisingly heterogeneous mixture of behaviors. Because the SA-β-Gal signal is graded and not binary (**Fig. 3.4**), we initially used a cutoff at the 95th percentile of untreated cells to designate a cell as SA-β-Gal-positive (hereafter SA-β-Gal^{pos}). Although most SA-β-Gal^{pos} cells were phospho-Rb^{low}, consistent with what would be expected for senescent cells, we also identified SA-β-Gal^{neg}/phospho-Rb^{high} cycling cells, SA-β-Gal^{neg}/phospho-Rb^{low} presumably quiescent cells, and a small fraction (1.7%) of unexpected SA-β-Gal^{pos}/phospho-Rb^{high} cells. This latter population calls into question the reliability of SA-β-Gal as a senescence marker, since no truly senescent cell should ever be in the cell-cycle (**Fig. 3.4**). However, comparing the relative intensities of SA-β-Gal staining following etoposide release revealed that the bluest cells in the population were significantly more likely to be phospho-Rb^{low} compared to less-blue cells, which were associated with more variability in phospho-Rb status (**Fig. 3.5**). This suggests that the confidence in classifying cells as senescent increases as a function of the intensity of SA-β-Gal staining, with

intermediate levels of SA-β-Gal staining encompassing both reversibly and irreversibly arrested cells.

To determine the origin of the SA-β-Gal^{pos}/phospho-Rb^{high} cells, we returned to our data set from Fig. 1.1E where the cells were also stained cells for SA-β-Gal at the end of the movie. Because SA-β-Gal^{pos}/phospho-Rb^{high} cells tended to have intermediate levels of SA-β-Gal staining, we hypothesized that this subpopulation might represent slow-cycling cells that we showed to be easily misclassified as senescent (**Fig. 3.1E**). To test this, we split the slow cycling subpopulation that re-entered the cell cycle during imaging into two categories: early vs. late escapers, based on whether the cells were Ki67^{off} or Ki67^{high} on the final frame of the movie (**Fig. 3.6, top**). As expected, we observed slow cycling cells that happened to be in the cell cycle at the final frame of the movie to have significantly higher levels of SA-β-Gal staining compared to untreated control cells, explaining the origin of the SA-β-Gal^{pos}/phospho-Rb^{high} subpopulation (**Fig. 3.6, bottom**). However, we detected no significant difference in the relative levels of blueness between the early and late escaping subpopulations, suggesting that past proliferative history rather than current cell-cycle status determines the eventual levels of SA-β-Gal staining (**Fig. 3.6, bottom**). Together, these data support two major conclusions: 1) cell cycle re-entry does not immediately extinguish SA-β-Gal staining, explaining the SA-β-Gal^{pos}/phospho-Rb^{high} subpopulation, and 2) SA-β-Gal positivity marks both reversibly and irreversibly arrested cell fates, rather than exclusively cellular senescence.

3.3.3 SA-β-Gal intensity scales with increased durations of cell-cycle withdrawal

To determine whether the overlap in SA-β-Gal staining between quiescent and senescent cells is due to the fact that its signal rises as a function of the duration of cell-cycle withdrawal, we filmed cells expressing a live-cell sensor for CDK2 activity[123] for days 6-10 following etoposide release (**Fig. 3.7A**). CDK2 activity begins to rise when cells commit to the cell cycle and increases steadily thereafter until mitosis, whereas cells turn off their CDK2 activity and enter a CDK2^{low} state when they exit the cell cycle. At the end of the time-lapse imaging on day 9, we fixed and

stained the cells for SA-β-Gal and mapped each cell's stain to its cell-cycle history over the previous four days (**Fig. 3.7B**). Binning cells into the top, middle, and bottom 10% of SA-β-Gal signal revealed that the intensity of staining was proportional to the total duration of time that cells spent out of the cell cycle in a $CDK2^{low}$ state. This shows that SA-β-Gal staining scales with increasing durations of cell-cycle withdrawal (**Fig. 3.7C, left**).

To test whether SA-β-Gal also has the resolution to identify cells withdrawn from the cell cycle due to low-grade endogenous stress[123], we quantified the intensity of SA-β-Gal staining in spontaneously quiescent cells in an unperturbed population. We sorted the bottom 1% of mCitrine-Ki67 signal by flow cytometry to enrich for the intrinsically slow-cycling cells in the population (**Fig. 3.7C right**). The cells were re-plated after sorting and their CDK2 activities were filmed over the subsequent two days. Cells designated SA-β-Gal^{pos} spent significantly more hours in the $CDK2^{low}$ state compared to SA-β-Gal^{neg} cells, supporting the notion that SA-β-Gal is a general readout of increased durations of cell-cycle withdrawal regardless of the stressor.

To extend these findings to multiple types of cell-cycle withdrawal, we measured the median SA-β-Gal signal in non-cycling cells after forcing cells into quiescence for 3, 6, 9, and 12d using four well-established methods: contact inhibition, serum starvation, CDK4/6 inhibition (Palbociclib), and Mek inhibition (Trametinib) (**Fig. 3.7D**). Unlike etoposide, these treatments induce a transient cell-cycle exit that reverses after washout[124], so increases in SA-β-Gal staining within the non-cycling cells stems from quiescent rather than senescent cells. Across all four treatment conditions, the SA-β-Gal signal increased as a function of treatment time (**Fig. 3.7E),** supporting the notion that SA-β-Gal is a graded marker whose signal intensity integrates the duration of time spent out of the cell cycle (**Fig. 3.7F**). We conclude that heterogeneity in SA-β-Gal staining is reflective of biological heterogeneity, where cells that cycle less often under stress accumulate more SA-β-Gal staining over time.

3.3.4 Increased SA-β-Gal staining reflects increased lysosomal content and autophagy

Why is SA-β-Gal staining is so closely coupled with cell-cycle status when the enzyme itself is dispensable for the induction and maintenance of senescence[121,125]? Since the β-galactosidase enzyme is localized to the lysosomes, we reasoned that increased SA-β-Gal staining could simply be a readout of increased lysosomal content, as has previously been reported but never displayed in single cells. To test this, we multiplexed measurements of SA-β-Gal and LAMP1, a membrane-embedded lysosomal protein, and found that they not only co-localized but the levels of both also simultaneously increased following acute chemotherapeutic stress (**Fig. 3.7G**). This reinforces the notion that increased lysosome biogenesis following cell stress leads to increased activity of β-galactosidase.

Next, we questioned whether the increased lysosome content following etoposide release was linked to changes in autophagy, since previous literature has suggested that senescent cells undergo increased autophagic flux to manage the accumulation of cellular damage [126]. To investigate this idea, we compared the autophagic flux in untreated and etoposide-released cells by comparing the relative increase in LC3II protein levels, a marker of autophagosome formation, following a 3h treatment of 50 μM chloroquine (CQ), a lysosomotropic agent that impairs autophagosome fusion[127]. Etoposide-released cells experienced a 2.2-fold increase in average LC3II protein levels following CQ treatment compared to control cells, which had a 1.5-fold increase. This result suggests that autophagy is significantly upregulated in cells released from acute chemotherapeutic stress (**Fig. 3.7H**).

To test whether increased SA-β-Gal staining is correlated with both increased lysosomal content and/or autophagic flux, we co-stained cells for SA-β-Gal and either LAMP1 or LC3II following etoposide release. As expected, the levels of both proteins were more significantly upregulated in cells with the highest levels of SA-β-Gal staining compared to cells with the lowest (**Fig. 3.7I**). Thus, SA-β-Gal staining reflects increased lysosomal content, which reflects increased autophagic flux in cells induced to senescence.

3.3.5 Increased SA-β-Gal staining reflects decreasing lysosomal efficiency

We combined the SA-β-Gal stain with both LysoTracker™, a fluorescent probe specific to the acidic environment of the lysosomes, and an antibody against LAMP1 and quantified the signals after treatment with bafilomycin A1. While both SA-β-Gal and LysoTracker™ staining were sensitive to lysosomal de-acidification by bafilomycin treatment, LAMP1 staining remained unaffected (**Fig. 3.8A-B**). This suggests that SA-β-Gal can be considered a readout of lysosomal activity, while LAMP1 is a readout of lysosomal content.

Because SA-β-Gal and LAMP1 staining are decouplable, we normalized the SA-β-Gal stain to lysosomal content to yield a lysosomal efficiency metric. We found that cells can have either high or low amounts of LAMP1 relative to SA-β-Gal staining, indicating low versus high lysosomal efficiencies, respectively (**Fig. 3.8C**). While these data recapitulate the observation that both SA-β-Gal and lysosomal content are elevated in cells induced to senescence[123], multiplexing these stains in single cells revealed decreasing lysosomal efficiency after etoposide release (**Fig. 3.8D**). Furthermore, as the population rebounded from genotoxic stress and resumed proliferation, the lysosomal efficiency returned to baseline because LAMP1 rises and falls faster than SA-β-Gal over the course of the 12d release (**Fig. 3.9**). A similar trend was observed for LysoTracker™ normalized to LAMP1 (**Fig. 3.9**). These data suggest that increased lysosomal content may represent a compensatory mechanism for decreasing lysosomal functionality in cells induced to senescence[128].

3.3.6 Lysosomal efficiency is impaired in deeply quiescent cells

Since SA-β-Gal staining appeared to be a readout of long durations of cell-cycle withdrawal (**Fig. 3.7**), we tested whether defects in lysosomal efficiency were intensified in deeply quiescent cells[128]. To compare cells at different quiescence depths, we serum starved cells for one or four weeks and subsequently filmed them for 72 hr after serum re-addition. One-week starved cells resumed proliferation earlier than four-week starved cells, indicating that the four-week starved cells are in a deeper quiescence than one-week starved cells (**Fig. 3.10, left**). Furthermore, 5% of one-week and 20% of four-week starved cells never re-entered the cell-

cycling during the window of filming, suggesting that a larger fraction of cells trend toward senescence with increasing starvation durations (**Fig. 3.10, left**). Cells starved for four weeks had significantly reduced lysosomal efficiencies compared to cells starved for one week, and non-cycling cells were more impaired than cycling cells in both conditions (**Fig. 3.10, middle**). These data suggest that decreasing lysosomal efficiency not only scales with increasing quiescence depth irrespective of cell-cycle re-entry time but also does not return to baseline levels immediately following cell-cycle re-entry (**Fig. 3.10, middle**). In other words, lysosomal efficiency does not reflect a cell's immediate past, but rather integrates the time spent out of the cell cycle over a longer period to drive different depths of quiescence (**Fig. 3.10, right**).

3.3.7 SA-β-Gal is diluted in large cells and concentrates over time

Different senescence markers manifest at different rates in senescent cells. Indeed, when we measured the relative SA-β-Gal signal over time we found that cells with the largest cytoplasmic areas accumulated the SA-β-Gal stain at a delayed rate compared to all cells, suggesting that the SA-β-Gal stain requires time to build up in the senescent subpopulation (**Fig. 11**). These data show that senescent cells are detected with increased confidence after population rebound begins to occur.

Furthermore, we questioned whether the delay in SA-β-Gal accumulation was caused by large cells being more diluted than small cells, a recently reported general feature of senescent cells[72,97]. Excessive cytoplasmic dilution causes a functional decline in the ability of cells to synthesize new RNA and protein[72,97], and this could explain the delay in the rise of SA-β-Gal in large cells over time. We therefore measured each cell's ratio of cytoplasmic area to DNA content after etoposide release and found that non-cycling pRb^{low} cells at 6d were indeed more dilute than untreated cells (**Fig. 3.12**). However, by 12d, the non-cycling subpopulation's dilution level began to return to baseline, indicating cellular re-concentration in the non-cycling cells over time (**Fig. 3.12**). To test whether cellular dilution plays a role in SA-β-Gal positivity, etoposide-released cells were separated by the top 10% and bottom 10% of SA-β-Gal signal and their cytoplasmic dilution

metrics and average protein abundance as measured by succinimidyl ester staining (18) were compared (**Fig. 3.13**). While SA-β-Gal^{high} cells were as concentrated as untreated cells, SA-β-Gal^{low} cells were the most dilute in the population (**Fig. 3.13**). Thus, heterogeneity in SA-β-Gal staining not only stems from differences in proliferation rate but also from variations in cellular concentration and protein expression, a previously reported feature associated with increased SA-β-Gal staining[61].

3.4 Discussion

Measuring senescence with either a single marker or at a single point in time can lead to incorrect conclusions about the biology or dynamics of senescent cells. To address these gaps, we used time-lapse imaging to differentiate quiescent cells that re-enter the cell-cycle from those that stay withdrawn, and we developed novel methods for multiplexing and quantifying that SA-β-Gal in single cells. These data revealed that increasing durations of cell-cycle withdrawal correlate with increasing SA-β-Gal intensity, increasing autophagy, and decreasing lysosomal efficiency.

SA-β-Gal has strengths and weaknesses as a marker of senescent cells due to its unique patterns of accumulation and decay over time. The stain accumulates in non-cycling cells as a function of time spent out of the cell cycle, and it builds up in large cells that re-concentrate their cellular material from a diluted state. Because the SA-β-Gal signal does not degrade immediately following cell cycle re-entry, slow-cycling cells can easily be mistaken as senescent since they can also be SA-β-Gal^{high}. This suggests that SA-β-Gal staining and lysosomal stress do not reflect a cell's immediate past but rather integrate information over a longer period. This means that long durations of quiescence in the past may be encoded by increased autophagy and reduced lysosomal function, which decreases the probability for cell cycle commitment.

While our data is consistent with previous studies that have shown autophagy to be activated in senescent cells[126], others have reported that autophagy is suppressed during irreversible arrest[74]. To explain these conflicting roles for autophagy in senescence, Khang and

Elledge, 2016 suggested that the SASP is promoted by the loss of specific autophagy, while general autophagy is upregulated to enhance cell survival and inhibit proliferation during senescence[126]. Despite this, the exact mechanism by which increased general autophagy decreases the probability of proliferation remains to be elucidated. Such insights could offer a more comprehensive understanding of how senescent cells maintain long-term cell-cycle arrest.

The most profound observation from this series of studies is that the gradation in SA-β-Gal staining encodes information about past proliferative history. Namely, cells that accumulate more SA-β-Gal signal spent longer durations withdrawn from the cell cycle for both quiescence and senescence-inducing treatments. These data suggest that senescence may represent the endpoint on a continuum of quiescence deepening; however, it is unclear whether other molecular markers of senescence could resolve a discrete "point of no return" for cell-cycle re-entry. An ideal marker for this irreversibility would be binary and have switch-like kinetics, rising only after commitment to permanent cell-cycle exit. Such a marker could not only contribute to developing more efficacious cancer therapies but also enhance the detection resolution for senescent cells *in vivo.*

3.5 Materials and Methods

3.5.1 Antibodies and reagents

pRb (S807/811) D20B12 XP (8516) was purchased from CST and used at a 1:500 dilution. Anti-human 53BP1 (612523) was purchased from BD and was used at a 1:1000 dilution. Alexa fluor secondary antibodies (A10521, A10520, A-21236, and A-21245) were all purchased from Thermo Scientific and used at 1:1000 dilutions. CF 488A succinimidyl ester (SCJ4600018) was purchased from Sigma and used at a 1:10,000 dilution. Hoechst 33342 was purchased from Thermo Scientific (H3570) and used at a 1:10,1000 dilution. The Senescence β-Gal Staining Kit was purchased from CST (9860). Etoposide (E1383) and chloroquine were purchased from Sigma (AAJ6445914). Palbociclib (S1116) and trametinib (S2673) were purchased from Selleckchem.

3.5.2 Cell lines and culture media

MCF10A (ATCC CRL-10317) cells were obtained from ATCC and grown in DMEM/F12 supplemented with 5% horse serum, 20 ng/ml EGF, 10 µg/ml insulin, 0.5 µg/ml hydrocortisone, 100 ng/ml cholera toxin, and 100 µg/mL of penicillin and streptomycin. MCF10A starvation media consisted of DMEM/F12, 0.5 µg/ml hydrocortisone, 100 ng/ml cholera toxin, and 100 µg/mL of penicillin and streptomycin. During live-cell imaging, phenol red-free full growth media was used. WI38-hTERT cells were grown in DMEM supplemented with 10% FBS and 100 µg/mL of penicillin and streptomycin. All cell lines were grown in a humidified incubator at 5% CO2 and 37 °C.

3.5.3 Drug treatments

MCF10A cells were plated at 100,000 cells per well in a plastic 6 well culture plate before being treated with 10 µM etoposide the following day for 24h. Etoposide was removed and cells were washed once with PBS before being returned to full growth media. The cells were maintained in culture throughout the duration of drug recovery with media refreshes every 3d. 24h prior to imaging, the etoposide-released cells were trypsinized and replated onto a collagen coated (1:50 dilution in water) (Advanced BioMatrix, No. 5005) 96-well glass-bottom plate (Cellvis Cat. No. P96-1.5H-N) at 1500 cells per well for live-cell imaging and 3000 cells per well for immunofluorescence. To induce quiescence, 1500 cells per well were plated directly onto a collagen coated 96-well glass-bottom plate and treated continuously with 3 µM Palbociclib, 100 nM Trametinib, or serum free media for up to 12 days. Contact inhibited cells were plated at 10,000 cells per well in full-growth media and cultured for up to 12 days. Media was refreshed on all the conditions every 3 days. To perturb autophagy, MCF10A cells were treated with 50 µM chloroquine 3h prior to fixing and staining.

3.5.4 Flow cytometry

MCF10A cells endogenously tagged with mCitrine-Ki67 and expressing H2B-mTurquoise and DHB-mCherry were trypsinized and resuspended in PBS + 1% FBS + 100 µg/mL of penicillin and streptomycin after a 5d recovery from a 24h treatment with 10 µM etoposide or 10 Gy of

ionizing radiation. Unlabeled wild-type cells were used to gate Ki67^{off} cells, which resulted in 25% of etoposide treated cells and 10% of IR treated cells being sorted and replated directly onto a collagen coated (1:50 dilution in water) (Advanced BioMatrix, No. 5005) 96-well glass-bottom plate (Cellvis Cat. No. P96-1.5H-N) for live-cell imaging that started the following day. As a control, the bottom 7.7% of untreated cells were also sorted and plated. For measuring SA-β-Gal in spontaneously quiescent cells, the bottom 1% of mCitrine-Ki67 was sorted and replated as described above for live-cell imaging that started 48h later.

3.5.5 Immunofluorescence

MCF10A cells were treated with 10 μM etoposide for 24h, washed, and allowed to recover before being seeded onto a collagen coated (1:50 dilution in water) (Advanced BioMatrix, No. 5005) 96-well glass-bottom plate (Cellvis Cat. No. P96-1.5H-N) 24h prior to fixation for 15 minutes with 4% PFA in PBS. Cells were permeabilized at room temperature with 0.1% TritonX for 15 minutes and blocked with 3% Bovine Serum Albumin (BSA) for 1h. Primary antibodies were incubated overnight in 3% BSA at 4 °C and secondary antibodies were incubated for 1-2h in 3% BSA at room temperature. Nuclei were labelled with Hoechst at 1:10,000 in PBS at room temperature for 15 min. Two 100 uL per well PBS washes were performed between each described step. All images were obtained using a 10x 0.4 numerical aperture objective on a Nikon TiE microscope.

3.5.6 Time-lapse microscopy

MCF10a cells were plated 24h prior to imaging and full growth media was replaced with phenol red-free full-growth media. Images were taken in CFP, YFP, and mCherry every 12 minutes at two sites per well that were spaced 2 mm apart. Total light exposure was kept below 600 ms. Cells were imaged in a humidified, 37°C chamber at 5% CO2. All images were obtained using a 10x 0.4 numerical aperture objective on a Nikon TiE microscope.

3.5.7 Image processing

Image processing and cell tracking were performed as previously described[118]. Phosho-Rb was separated into high and low modes by using the saddle-point in the data as the cutoff. Ki67off cells were classified as those less than the 95th percentile of the median nuclear signal in WT cells. Nuclear signals were quantified from a nuclear mask, which was generated using Otsu's method on cells stained for Hoechst. Cytoplasmic signals were quantified from a cytoplasmic mask, which was generated using Otsu's method on cells stained for succinimidyl ester. The regionprops function in MATLAB was used to quantify the mean signal for each stain from binary masks of the nucleus or cytoplasm. Immunofluorescence and SA-β-Gal signals were linked back to live-cell imaging traces by nearest neighbor screening after jitter correction as previously described[118].

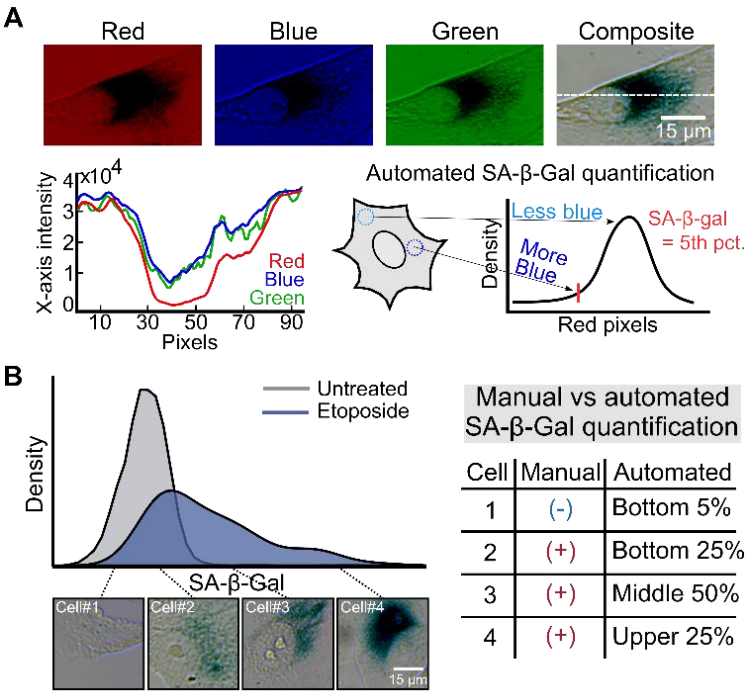

Figure 3.1 A novel method for quantifying SA-β-Gal staining (A) A representative single MCF10A cell stained for SA-β-Gal and imaged in pseudo-color-brightfield at 6d after release from 10 µM etoposide for 24h. An intensity profile (dotted line) was taken from each channel of the RGB stack. We define the SA-β-Gal signal as the 5th percentile of the red pixels in the cytoplasm of each cell. (B) Distribution of SA-β-Gal signal after etoposide release with 4 representative single cells at increasing intensities of staining.

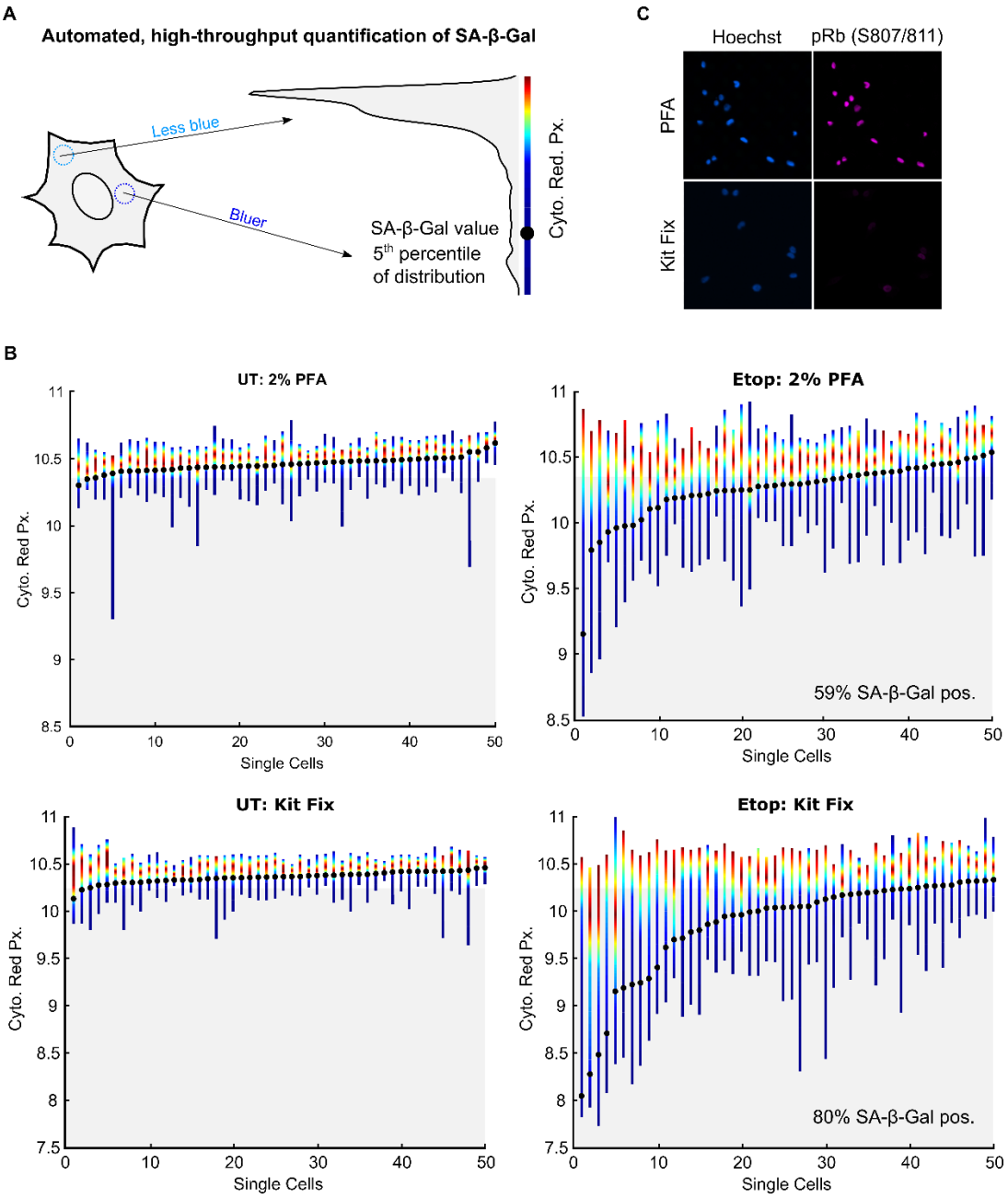

Figure 3.2 Automated, high-throughput quantification of the SA-β-Gal stain in single cells induced to senescence (A) A single representative cell's cytoplasmic red pixel distribution. The heatmap corresponds to the relative frequency of events along the distribution. (B) Quantification of SA-β-Gal for 50 single cells left untreated or released for 6d from a 24h treatment with 10 μM etoposide, for both 2% PFA (which is optimal for immunofluorescence + SA-β-Gal) and the CST kit fixative (which is optimal for detection of SA-β-Gal). The black dot is the value at the 5th percentile of the distribution, which is the SA-β-Gal score for that cell. The percentage of SA-β-Gal^{pos} cells was calculated using the 95th percentile of all untreated cells as the cutoff. Heatmap coloring as in panel A. (C) Comparison of immunofluorescence for phospho-Rb (S807/811) after fixation with 2% PFA versus CST SA-β-Gal kit fixative in WT MCF10A cells showing the weaker immunofluorescence signal with the CST kit fixative.

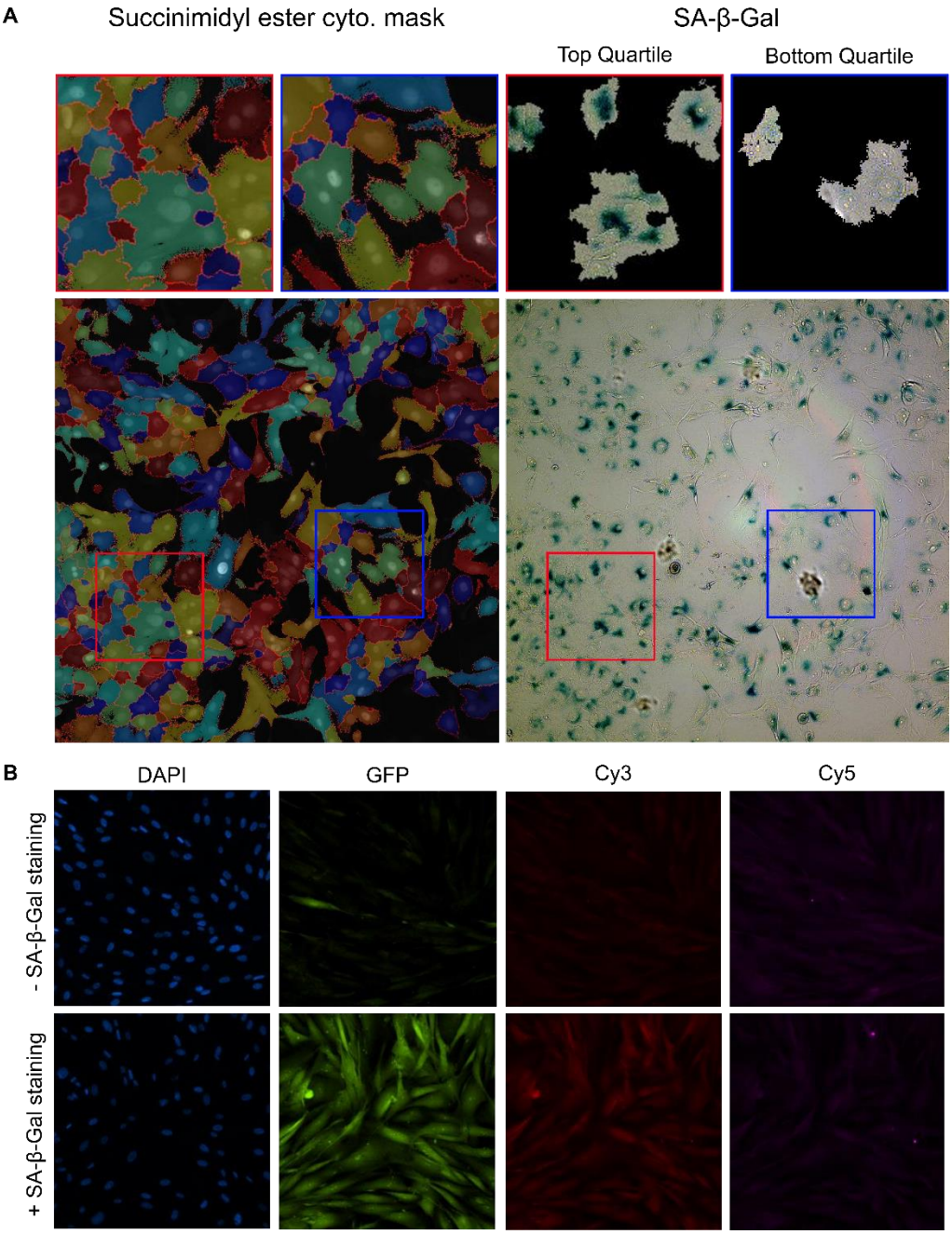

Figure 3.3 Validation of the SA-β-Gal quantification method and comparison of background fluorescence (A) Validation of whole-cell segmentation using the succinimidyl ester stain and SA-β-Gal quantification by displaying the upper and lower quartiles of SA-β-Gal signals from the binary cytoplasmic mask after a 4d release from a 24h pulse of 10 μM etoposide in MCF10A cells. (B) Comparison of background fluorescence after secondary antibody staining in each fluorescent channel with and without co-staining WI38 cells for SA-β-Gal (kit fixative).

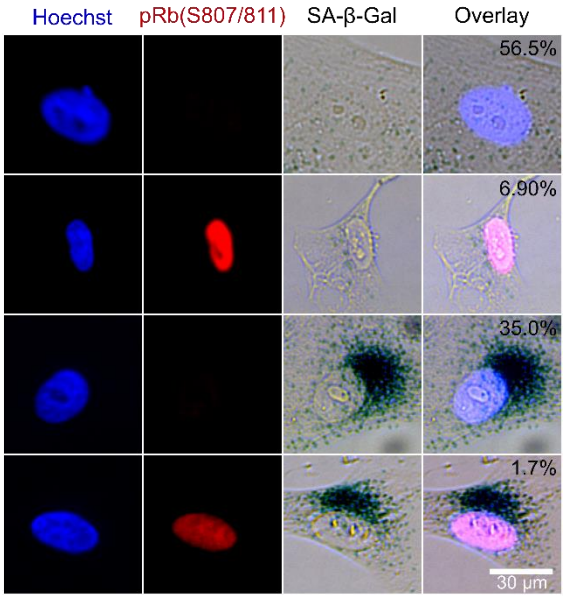

Figure 3.4 SA-β-Gal and phospho-Rb co-staining Heterogeneity in co-staining of SA-β-Gal and Rb phosphorylation by immunofluorescence in MCF10A cells released for 6d from a 24h treatment with 10 μM etoposide. Percentages reflect the fraction of cells with each behavior.

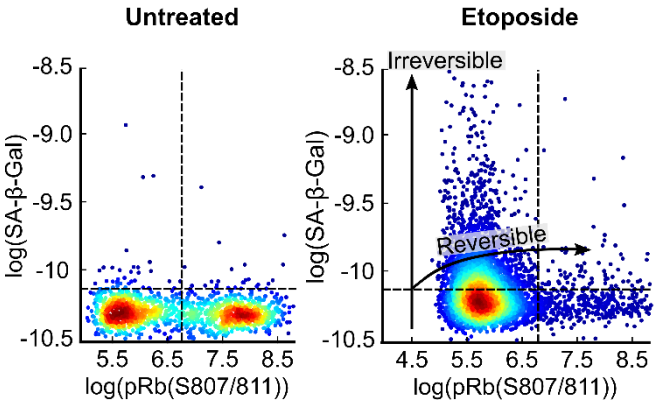

Figure 3.5 SA-β-Gal and phospho-Rb co-staining quantification Scatter plots of SA-β-Gal versus phospho-Rb from the same cells in Fig. 3.4. The arrows indicate the hypothesized quiescence versus senescence cell fate trajectories based on the level of SA-β-Gal.

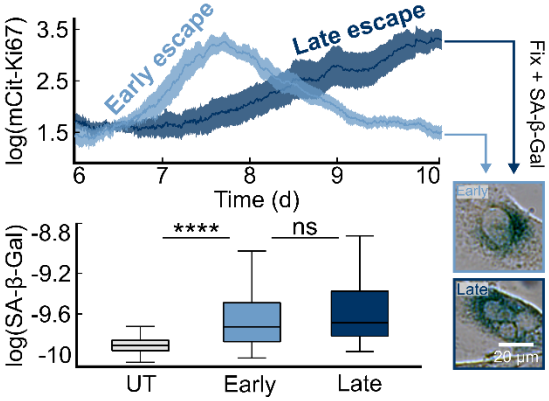

Figure 3.6 SA-β-Gal persists even upon cell-cycle re-entry in slow-cycling cells The same data in Fig. 1.1E for etoposide-released cells that entered the cell cycle during live-cell imaging. Early escaping cells were those that were Ki67^{off} on the final frame of the movie while late escaping cells were those that were Ki67^{high} on the final frame of the movie. Single-cell traces were linked back to their relative SA-β-Gal levels after being fixed and stained for the marker at the end of imaging.

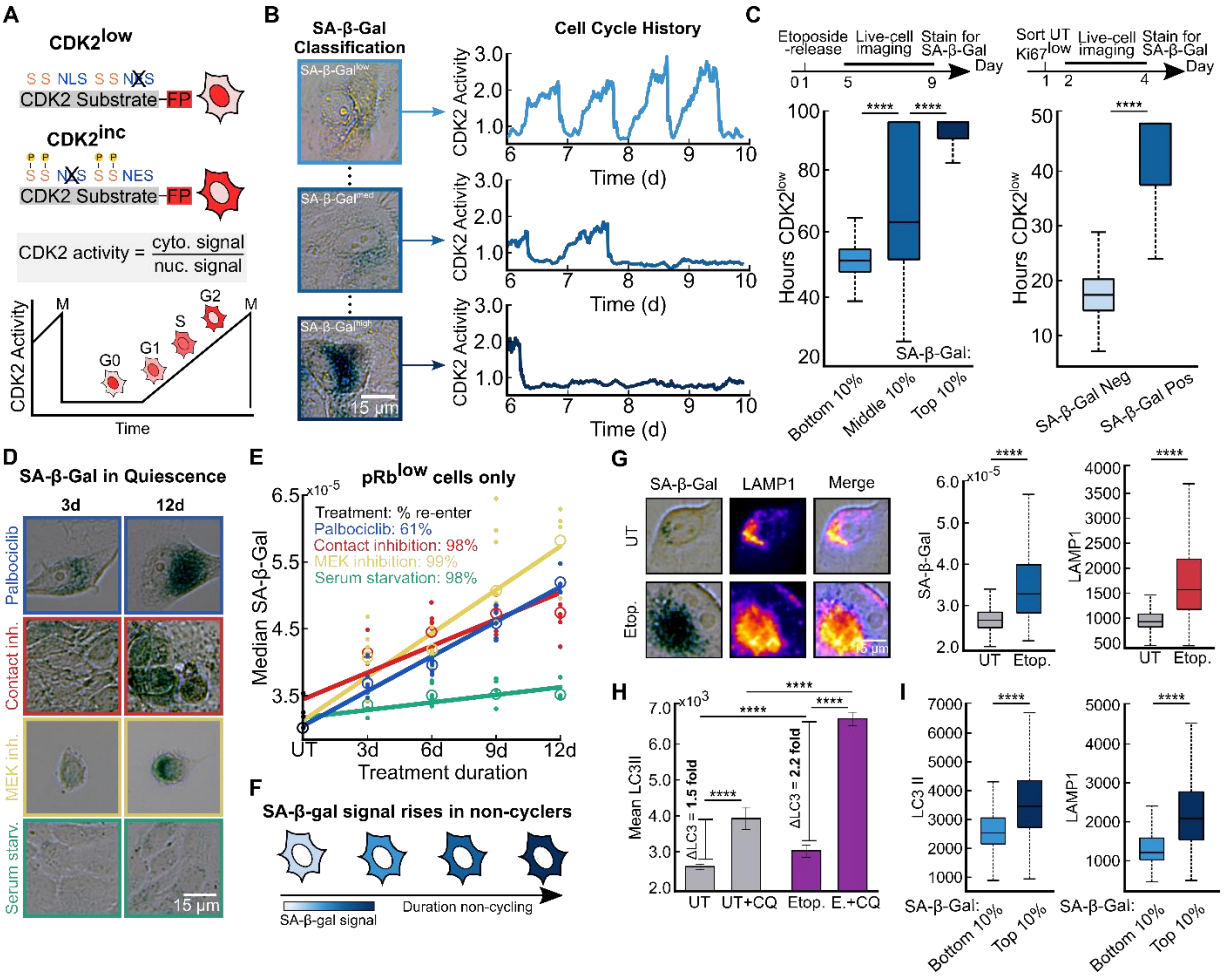

Figure 3.7 SA-β-Gal staining marks long durations of cell cycle exit and is correlated with increased lysosomal content and autophagic flux (A) Schematic of the CDK2 activity sensor. The sensor localizes to the nucleus when unphosphorylated; progressive phosphorylation by CDK2 leads to translocation of the sensor to the cytoplasm. NLS, nuclear localization signal; NES, nuclear export signal; S, CDK consensus phosphorylation sites on serine. (B) MCF10A cells expressing the CDK2 activity sensor were treated with 10 μM etoposide for 24h, washed, and subjected to time-lapse microscopy 5d later for 96h (from 5d-9d). The cells were fixed and stained for SA-β-Gal after the last frame was taken; (C: left) single-cell traces were clustered based on the top, middle, and bottom 10% of SA-β-Gal signal and the total hours CDK2^{low} (below a cutoff of 0.8) was plotted for each bin. (C: right) Untreated MCF10A cells were sorted by flow cytometry for the bottom 1% of mCitrine-Ki67 signal, plated and allowed to grow for 48h, filmed for 48h to monitor CDK2 activity, fixed and stained for SA-β-Gal, and were manually classified as SA-β-Gal positive versus negative. (D-E) MCF10a cells were pushed into quiescence by contact inhibition, serum starvation, 3 μM Palbociclib treatment, or 100 nM Trametinib treatment for 3-12d and fixed and stained for SA-β-Gal and phospho-Rb. Best fit lines were computed for each condition from the average of 6 technical replicates. Percentages are the proportion of cells that re-enter the cell cycle after a 5d release from 2 weeks of treatment. (F) Model for SA-β-Gal accumulation as a function of cell-cycle exit time. (G) MCF10A cells were treated with 10 μM etoposide for 24h, washed, fixed after 3d, and stained for SA-β-Gal and LAMP1. (H-I) Same experimental scheme as described in Fig. 3G. Cells were fixed and stained for SA-β-Gal, LC3II, and LAMP1 after a 3 h treatment with 50 μM chloroquine.

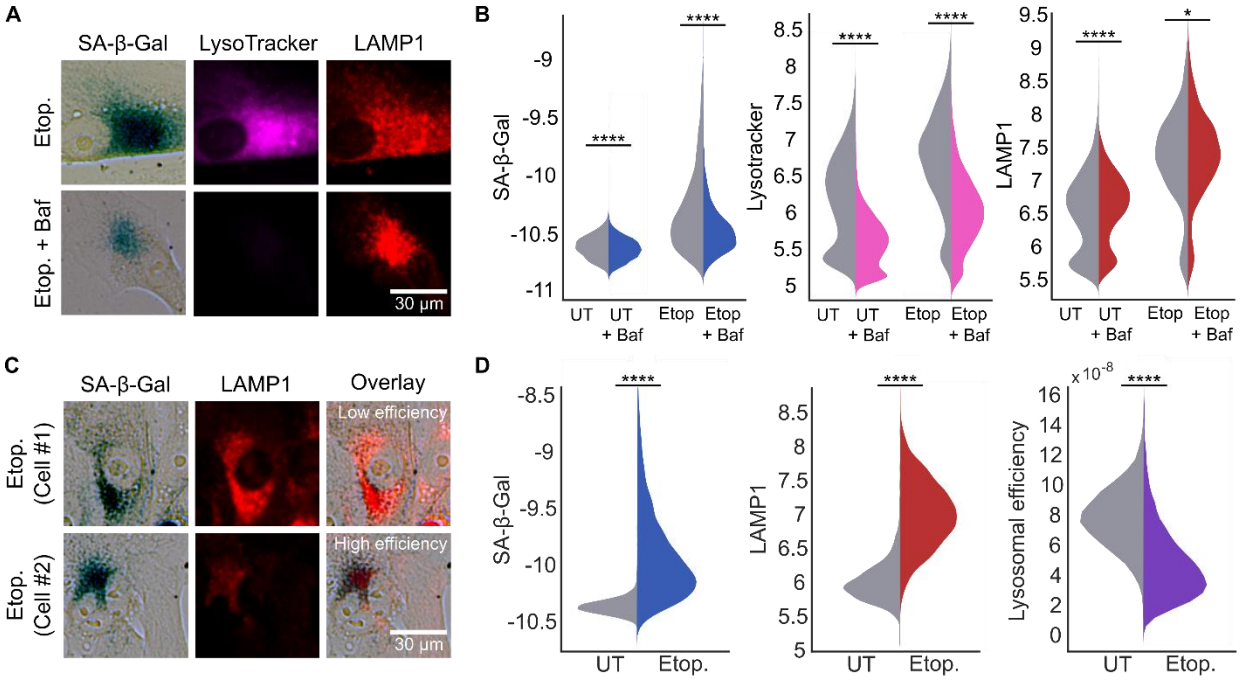

Figure 3.8. SA-β-Gal staining reflects increased lysosomal content but decreased lysosomal function (A) Representative MCF10A cells treated with 10 μM etoposide for 24 hr, washed, fixed after 5d, and stained for SA-β-Gal. Prior to fixing, cells were treated with 100 nM Bafilomycin A1 (Baf) for 1.5 hr followed by a combination 100 nM Baf A1 + LysoTracker™ for an additional 1.5 hr. (B) Quantification of cells from A. (C) Representative cells treated with 10 μM etoposide for 24 hr, washed, fixed after 5d, and stained for SA-β-Gal and LAMP1, showing heterogeneity of LAMP1 staining in SA-β-Gal^{high} cells. (D) Calculation of lysosomal efficiency obtained by dividing each cell's SA-β-Gal signal by its LAMP1 signal.

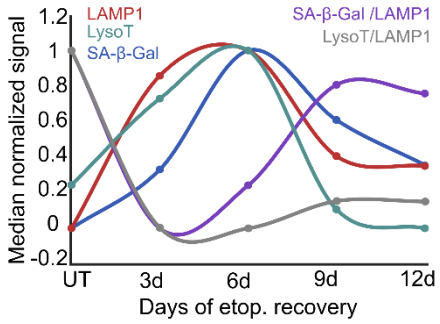

Figure 3.9. Kinetics of SA-β-Gal, LysoTracker, and LAMP1 over time after release from etoposide Cells were treated with 10 μM etoposide, washed, fixed after the indicated number of days, and stained for SA-β-Gal, LAMP1, and LysoTracker™. Note that proliferation begins to rebound after 5d.

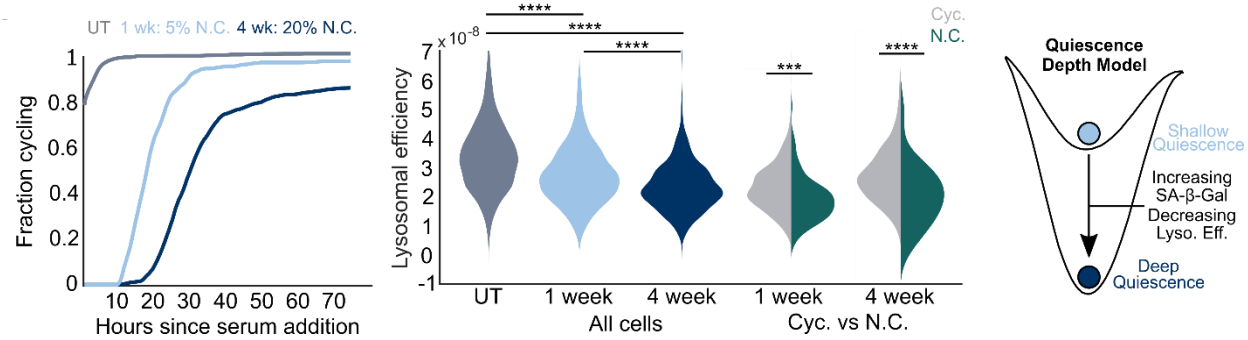

Figure 3.10. Lysosomal function is impaired in deeply quiescent cells (Left) MCF10A cells were serum starved for one or four weeks, restimulated with serum, filmed for 3d to monitor their CDK2 activity, fixed, and stained for SA-β-Gal and LAMP1 at the end of the movie (n=50 in each plot). (Middle) Left: cumulative fraction of cells that re-enter the cell cycle. The fraction of cells that had not re-entered the cell-cycle by the end of the movie is: UT (0%); 1wk (5%); 4wk (20%). Right: lysosomal efficiency was calculated for untreated (gray), 1-week (light blue), and 4-week (dark blue) serum-starved cells; the 1-week and 4-week data are then displayed as split violins for cells that re-entered the cell-cycle (Cyc.) versus those that remained non-cycling throughout filming (N.C.). (Right) Model for quiescence depth after serum starvation adapted from Fujimaki et al.

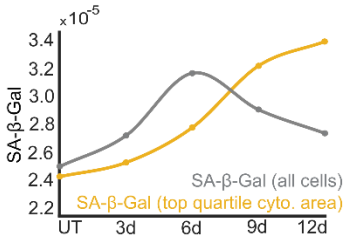

Figure 3.11. SA-β-Gal continues to rise in the largest cells in the population SA-β-Gal signal was measured over the course of a 12d recovery after release from a 24 hr pulse of 10 μM etoposide treatment in all cells versus cells in the top quartile of cytoplasmic areas.

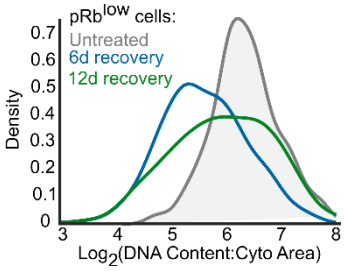

Figure 3.12. Non-cycling cells released from etoposide re-concentrate their contents over time Cytoplasmic dilution was calculated in the pRblow subpopulation as the ratio of DNA content (using Hoechst) to cytoplasmic area (using succinimidyl ester) at 6d versus 12d after release from a 24 hr pulse of 10 μM etoposide.

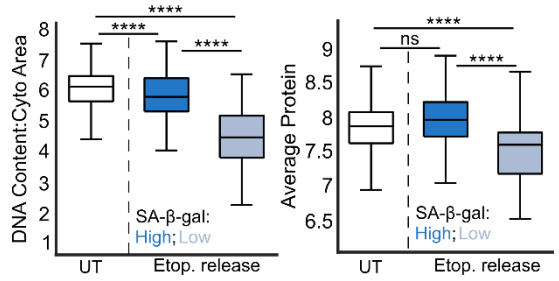

Figure 3.13. SA-β-Gal staining reflects increased cellular concentration The ratio of DNA content to cytoplasmic area and the average protein (average of succinimidyl ester) were plotted for the top and bottom 10% of SA-β-Gal signals at 6d after release from a 24 hr pulse of 10 μM etoposide.

Chapter 4

The intensities of senescence biomarkers integrate the duration of cell-cycle withdrawal

4.1 Abstract

Senescence, a state of permanent cell-cycle withdrawal, is difficult to distinguish from quiescence, a transient state of cell-cycle withdrawal. This difficulty arises because quiescent and senescent cells are defined by overlapping biomarkers, raising the question of whether these states are truly distinct. To address this, we used single-cell time-lapse imaging to distinguish cells that cycle very slowly from cells that never cycle at all after recovery from acute DNA damage, followed by staining for various senescence biomarkers. We found that the staining intensity of multiple senescence biomarkers is graded rather than binary and primarily reflects the duration of cell-cycle withdrawal, rather than senescence per se. Together, our data show that quiescent and senescent cells are nearly molecularly indistinguishable from each other at a snapshot in time, suggesting that cell-cycle withdrawal itself may be graded rather than binary, where the intensities of senescence biomarkers reflect the likelihood of cell-cycle re-entry.

4.2 Introduction

Correct identification of senescent cells is important in several clinical contexts, including the development of senolytic treatments to eliminate aged and damaged cells, as well as in the context of cancer chemotherapy where the abundance of quiescent vs. senescent states have opposing implications for tumor relapse[90,104,129,130]. However, quiescent and senescent cells are challenging to distinguish at a snapshot in time, making it unclear how to determine whether cell-cycle arrest is irreversible. This issue is exacerbated by the fact that cells have an impaired ability to re-enter the cell cycle from an arrested state if they spend longer amounts of time out of the cell cycle, suggesting that cell-cycle withdrawal is graded rather than binary. These cells have been termed “deeply quiescent” and are speculated to eventually transition into senescence if exited from the cell cycle for long enough[93,128]. If this is the case, it implies that quiescence and

senescence are not distinct cellular states but rather discrete points along a continuum of cell-cycle withdrawal, where reversibly and irreversibly arrested cells have overlapping molecular hallmarks. Alternatively, the switch from reversible to irreversible arrest may trigger the activation of specific signaling cascades that allow quiescent and senescent cells to have unique cellular functions that may be the targets for future cancer and aging therapies. Comparing these outcomes has been challenging since no study has systematically tested these markers against a ground-truth readout of senescence to quantify their predictive power for identifying senescent versus quiescent cells. To do this, multiplexing multiple markers in single cells has been suggested as a new goal to identify senescent cells more accurately[120,131]. In addition to SA-β-Gal staining, include the lack of cell-cycle markers (e.g. Ki67 and phospho-Rb), expression of Cyclin-Dependent Kinase (CDK) inhibitors (e.g. p21 and p16), DNA damage (e.g. 53BP1 or γH2AX), presence of the senescence-associated-secretory phenotype (SASP, with IL6 and IL8 being among the most common factors), loss of Lamin B1 (a structural component of the nuclear lamina[76]), and increased cell size[120,131]. However, these markers are often used qualitatively and subjectively, causing uncertainty among scientists and clinicians about how to most accurately define senescent cells, making it worthwhile to revisit this topic with updated single-cell tools.

4.3 Results

4.3.1 Canonical senescence biomarkers resolve cycling from non-cycling cells better than they resolve quiescent from senescent cells

Because SA-β-Gal staining scaled with increased durations of cell-cycle withdrawal, we next asked whether other markers of senescence follow the same trend. To test this, we measured SA-β-Gal, LAMP1, cytoplasmic area, nuclear area, IL8 protein, 53BP1 (a protein that forms foci at sites of DNA damage)[116], p21, and Lamin B1 from 6-10 days after etoposide release. First, we classified cells as either fast-cycling, slow-cycling, or predicted-senescent based on the number of hours spent in the CDK2low state (**Fig. 4.1A and Fig. 4.2A-B**), with predicted-senescent cells being defined as those that were CDK2low for the entire movie. For the first 7

markers, the intensity of staining was highest for predicted-senescent cells, intermediate for slow-cycling cells, and lowest for fast-cycling cells, while Lamin B1 followed the opposite trend (**Fig. 4.2C**).

Second, we grouped cells based on marker staining intensity into the top, middle, and bottom 10% and plotted the time the cells had spent in the CDK2low state over the prior 4 days. For each marker, a graded trend was observed, where the intensity of staining of the marker was correlated with the duration withdrawn from the cell cycle, with Lamin B1 again following the opposite trend compared to the others (**Fig. 4.2D**). These data suggest that the relative intensities of canonical senescence biomarkers encode, in a snapshot, information about the cell-cycle histories of single cells released from acute DNA damage.

To quantitatively compare the powers of these senescence markers to accurately identify predicted-senescent cells, we generated receiver operating characteristic (ROC) curves for each of the markers. The ROC curve compares the true positive rate versus the false positive rate at increasing thresholds of detection, where high thresholds maximize true-positive and low thresholds minimize false negatives. In this case, we classified cells as true positives if they remained CDK2low throughout the duration of the movie, which we approximated to be the true senescent subpopulation. For each marker, we computed 2 ROC curves: the first was for all cells in the population while the second was for only slow-cycling and predicted-senescent cells. This analysis allowed us to compare the relative resolving power for each senescence biomarker to differentiate 1) predicted-senescent cells from all other cells and 2) predicted-senescent from slow-cycling cells that pass through long periods of quiescence. Unsurprisingly, predicted-senescent cells are more easily resolved from fast-cycling cells than they are from slow-cycling cells that occasionally re-enter the cell cycle (**Fig. 4.2E**). Importantly, SA-β-Gal had the lowest ability to separate predicted-senescent cells from slow-cycling cells according to the ROC analysis (area-under-the-curve (AUC) = 0.55), whereas p21 and Lamin B1 had the highest ability to detect predicted-senescent cells (AUC=0.75-0.76), with the other markers falling in between.

Next, we pooled all single-cell traces for each marker and binned cells into seven groups based on how many hours they spent in the CDK2low state during live-cell imaging from 6-10d after etoposide release. We then averaged the intensity of each marker in each bin and plotted the result as a heatmap (**4.3, left and Fig. 4.4**). This analysis clearly displays the graded nature of the increase (or decrease for Lamin B1) in marker intensities as a function of time spent withdrawn from the cell cycle in response to etoposide treatment.

To test whether these results are generalizable to other types of senescence induction, we performed a similar experiment using hydrogen peroxide to induce oxidative stress, a common treatment for inducing senescence[132]. Here, cells were released from a 2hr treatment of 100 μM hydrogen peroxide and then immediately imaged for 4 days before being fixed and stained for the same senescence biomarkers. Although the percentage of predicted-senescent cells was lower after peroxide release than after etoposide release, we found a similar graded pattern in the staining of each marker with respect to cell-cycle status (**Fig. 4.1B, Fig. 4.3, right and Fig. 4.4**). These results indicate that our findings can generally be extended to additional methods of senescence induction and are independent of the level of population heterogeneity.

4.3.2 Multiplexing senescence markers in single cells increases the resolution for detecting non-cycling cells

While all the markers we assessed exhibited a graded increase in expression levels with respect to cell-cycle withdrawal time, p21 and Lamin B1 demonstrated the high discriminative power in our ROC analysis (**Fig. 4.2E**). We hypothesized that the reason for this could be that the levels of p21 and Lamin B1 rapidly revert to their baseline intensities following cell-cycle re-entry, causing slow-cycling cells to reset their signals periodically compared to predicted-senescent cells. To test this idea, we compared the mean signal of p21 and Lamin B1 in slow-cycling cells that were in the cell cycle on the final frame of the movie vs. those that were withdrawn from the cell cycle at the end of filming. This allowed us to decouple the effects of current cell-cycle status from past proliferative history on the intensity of senescence biomarker staining. Consistent with

our hypothesis, p21 levels fell immediately upon cell-cycle re-entry, consistent with prior time-lapse imaging of endogenously tagged p21[11], and Lamin B1 levels rose immediately upon cell-cycle re-entry (**Fig. 4.5A**). Thus, p21 and Lamin B1 "forget" the duration of cell-cycle withdrawal quickly, supporting the hypothesis that p21 and Lamin B1 can resolve predicted-senescent cells from slow-cycling cells because high levels of p21 and low levels of Lamin B1 are only achieved from long, continuous durations of cell-cycle withdrawal.

Next, we tested whether multiplexing the two markers with the highest AUC in Fig. 4C could increase our ability to identify cells that never cycled throughout the duration of imaging, which we classify as the predicted-senescent cells. After live-cell imaging from 6-10d following 10 μM etoposide release, we co-stained cells for p21 and Lamin B1 (**Fig. 4.5B**). We also computed each cell's nuclear area, which we obtain for free from the time-lapse analysis (**Fig. 4.5B**). In order to have enough cells to assess the marker triple-plex, we applied generous thresholds for each marker by taking the top quartile of signal for p21 and nuclear area and the bottom quartile of signal for Lamin B1. With these cutoffs, p21 alone, nuclear area alone, and Lamin B1 alone correctly identified predicted-senescent cells 57%, 70%, and 75% of the time (**Fig. 4.5C, left**). The reason p21 performs worse than Lamin B1 and nuclear area is because this analysis uses a single threshold, the top or bottom quartile, whereas the ROC analysis scans all possible thresholds. Combining p21 and Lamin B1 raised the percent of cells correctly predicted to 83%, and adding in nuclear area raised this value to 91% (**Fig. 4.5C, left**). The false-positive rate (flagging cells as senescent when they were not) followed the inverse trend (**Fig. 4.5C, right**).

While these data show that combining multiple markers in single cells increases the correct identification of predicted-senescent cells, it remains unclear which marker combinations and at which signal intensities the highest proportion of predicted-senescent cells can be captured. To determine this, we performed several local polynomial regression analyses for each combination of marker pairings against the duration spent CDK2low throughout filming. This allowed us to generate several 3D surface projections whose topologies represent the

proliferative likelihood of cells at different intensities of staining for each marker (**Fig. 4.5D**). From this, we found that as the intensities of any pair of markers rose (or fell for Lamin B1), the duration spent CDK2low increased proportionally, supporting our previous observation that senescence biomarker intensity at a snapshot encodes the proliferative history of single cells (**Fig. 4.2 and Fig. 4.3**).

Lastly, we investigated whether the source of heterogeneity in marker staining could be associated with different levels of DNA damage, which in turn may directly influence the extent of p21 induction. Although our ROC analysis did not reveal a large distinction between slow-cycling and predicted-senescent cells with 53BP1 staining, we suspected that this could be due to the discrete nature of this marker (i.e. cells can only have an integer number of foci). Despite these limitations, we multiplexed 53BP1 with p21 and nuclear area after a 6d release from a 24h treatment of 10 μM etoposide. Indeed, binning cells into the number of 53BP1 foci revealed that the number of 53BP1 foci scales with both p21 (**Fig. 4.6A**) and nuclear area (**Fig. 4.6B**), suggesting that heterogeneity in DNA damage gives rise to a gradient in the staining intensity of these two biomarkers. This is consistent with the fact that DNA damage activates p53, which upregulates p21[41,133] and with the notion that DNA damage can cause cells to slip from G2 to G1 phase without mitosis, creating large 4N DNA content cells[134].

4.3.3 The largest cells in the population go on to accumulate features of truly senescent cells

In addition to the duration of cell-cycle withdrawal, it was recently reported that increased cell size, one of the first identified and most universally upregulated markers of senescence[66], is causal for the enrichment/ depletion of numerous molecular markers[72,73]. In this model, imbalanced scaling of the proteome causes some proteins to superscale with size (E.g. SA-β-Gal and LAMP1) while other proteins subscale with size (E.g. Lamin B1)[70,73]. To reconcile our findings in context of these observations, we returned to our dataset from Fig. 2.1D where untreated and etoposide-released mCitrine-Ki67 MCF10A cells were sorted to be Ki67off and replated for

timelapse imaging the following day. Cells were classified as fast (untreated yet Ki67^{off} at the time of sorting), slow (etoposide-released and re-entered the cell cycle before the movie ended), or predicted-senescent (etoposide-released and remained predicted-senescent Ki67^{off} throughout the movie), and their mean nuclear areas were compared in the first 10h of filming when every cell was still Ki67off, since nuclear area correlates well with cell size (**Fig. 4.6A**)[135,136]. Predicted-senescent cells were significantly larger than slow-cycling cells, which were significantly larger than fast-cycling cells in the 10h window preceding escape from the Ki67off state (**Fig. 4.6A, right**), reinforcing the notion that increased cell size may be a driver for reduced cell-cycle re-entry.

Furthermore, because the largest cells in the population at a snapshot were more likely to remain arrested into the future, we questioned whether increased cell size was linked to a higher intensity of staining of canonical senescence markers over time. To test this, we measured SA-β-Gal, LAMP1, IL6 by mRNA fluorescence in situ hybridization (FISH), 53BP1, p21, and Lamin B1 at 6d and 12d following a 24h treatment of 10 μM etoposide and compared the distributions for all cells versus the largest cells in the population (**Fig. 4.6B**). For the first 5 markers, the entire population rose and fell along the duration of recovery, since fast-cycling cells eventually outgrew predicted-senescent cells; however, within the subset of “large” cells, the intensities of the markers continuously increased over time, while Lamin B1 followed the opposite trend (**Fig. 4.6B**). Thus, the largest cells following etoposide release accumulate a canonical senescent phenotype overtime, while the remainder of the population re-enters the cell cycle and contributes to population regrowth.

4.4 Discussion

In this study, we measured the intensities of several senescence biomarkers following etoposide release and found that SA-β-Gal staining was not the only marker whose intensity was linked to a decreased likelihood for proliferation. Indeed, increased cell size, LAMP1 staining, IL8, 53BP1 foci number, p21, and Lamin B1 were also strongly correlated with a reduction in the

proliferative fate of single cells (**Fig. 4.4**). Among these markers, p21 and Lamin B1 had the highest resolving power for non-cycling cells compared to slow-cycling cells, since their signal intensities were highly sensitive to recent cell-cycle re-entry (**Fig. 4.5**). Together, our data suggest that withdrawal from the cell cycle is not a binary fate; rather, it exists on a continuum, where the probability to proliferate is strongly associated with the intensities of senescence markers.

This lack of clarity among cells at varying depths of cell-cycle exit has been reported extensively in recent literature. Most notably, Fujimaki, 2019 found that longer withdrawal from the cell cycle by serum starvation leads to a transcriptomic profile that increasingly resembles that of senescent cells, suggesting that reversible and irreversible cell-cycle exits are on a continuum[128]. Additionally, Stallaert, 2022 applied dimensionality reduction methods from hyperplexed imaging data of many cell cycle regulators after both quiescence and senescence induction and identified several graded arrest trajectories[32]. They noted heterogeneity among non-proliferative cells across multiple established markers of arrest, where the cells with the highest staining intensity were the furthest from proliferating cells in high dimensional space[32]. These observations strongly support our findings that cell-cycle withdrawal is graded rather than binary, where the likelihood of cell proliferation is strongly linked to the intensities of senescence markers. Furthermore, because irreversible withdrawal from the cell cycle is not a prerequisite for cells to stain positive for senescence markers, the biological importance of distinguishing long arrest from permanent arrest following senescence induction remains unclear.

Finally, while our findings indicate a strong correlation between the duration of cell-cycle withdrawal and senescence marker staining, others have suggested that dysregulated cell size, due to imbalanced proteome scaling, plays a causal role in the induction of these markers [73,137,138]. Consistent with this notion, we identified that the largest cells in the population go on to accumulate features of truly senescent cells (**Fig. 4.7**) with extended durations of recovery from acute DNA damage, suggesting that increased cell size reinforces a reduced capacity for proliferation. However, this relationship works both ways, as constraining cell size during

senescence induction decreases the abundance of tumor suppressor proteins [137], indicating that increased cell size, the duration of cell-cycle arrest, and the intensity of senescence biomarker staining are phenotypically and molecularly coupled.

Future studies with the ability to classify cells as reversibly vs. irreversibly arrested at a snapshot in time will be critical for establishing more universal definitions for quiescence and senescence. This would help clarify the functional importance of the quiescent subpopulation that emerges alongside senescent cells after etoposide release, since our study calls into question the link between irreversible arrest and expression of senescence markers.

4.5 Materials and Methods

4.5.1 Antibodies and reagents

Anti-Ki67 (ab15580) and LC3 II (ab192890) were purchased from Abcam and used at 1:2000 and 1:1000 dilutions. pRb (S807/811) D20B12 XP (8516), LAMP1 D2D11 XP (9091), p21 Waf1/Cip1 (12D1) (2947), and Lamin B1 (D9V6H) (13435) were purchased from CST and used at 1:500, 1:1000, 1:250, and 1:1000 dilutions. Anti-human 53BP1 (612523), Purified Mouse Anti-Human IL-8 (550419), and Waf1/Cip1/CDKN1A p21 (SX118) (sc-53870) were purchased from BD and were used at a 1:1000 dilution. LAMP1 (sc-20011) was purchased from Santa Cruz Biotech and used at a 1:1000 dilution. Alexa fluor secondary antibodies (A10521, A10520, A-21236, and A-21245) were all purchased from Thermo Scientific and used at 1:1000 dilutions. IL6 FISH mRNA probe set (VA6-12712-VC) was purchased from Thermo Scientific. CF 488A succinimidyl ester (SCJ4600018) was purchased from Sigma and used at a 1:10,000 dilution. Hoechst 33342 was purchased from Thermo Scientific (H3570) and used at a 1:10,1000 dilution. The Senescence β-Gal Staining Kit was purchased from CST (9860). The ViewRNA ISH Cell Assay Kit was purchased from Thermo Scientific (QVC0001). Etoposide (E1383), Hydrogen Peroxide (108600) Chloroquine (AAJ6445914), and Brefeldin A (B7651) were purchased from Sigma.

4.5.2 Cell lines and culture media

MCF10A (ATCC CRL-10317) cells were obtained from ATCC and grown in DMEM/F12 supplemented with 5% horse serum, 20 ng/ml EGF, 10 µg/ml insulin, 0.5 µg/ml hydrocortisone, 100 ng/ml cholera toxin, and 100 µg/mL of penicillin and streptomycin. During live-cell imaging, phenol red-free full growth media was used. All cell lines were grown in a humidified incubator at 5% CO2 and 37 °C.

4.5.3 Drug treatments

MCF10A cells were plated at 100,000 cells per well in a plastic 6 well culture plate before being treated with 10 µM etoposide the following day for 24h. Etoposide was removed and cells were washed once with PBS before being returned to full growth media. The cells were maintained in culture throughout the duration of drug recovery with media refreshes every 3d. 24h prior to imaging, the etoposide-released cells were trypsinized and replated onto a collagen coated (1:50 dilution in water) (Advanced BioMatrix, No. 5005) 96-well glass-bottom plate (Cellvis Cat. No. P96-1.5H-N) at 1500 cells per well for live-cell imaging and 3000 cells per well for immunofluorescence.

4.5.4 Immunofluorescence

MCF10A cells were treated with 10 µM etoposide for 24h, washed, and allowed to recover before being seeded onto a collagen coated (1:50 dilution in water) (Advanced BioMatrix, No. 5005) 96-well glass-bottom plate (Cellvis Cat. No. P96-1.5H-N) 24h prior to fixation for 15 minutes with 4% PFA in PBS. Cells were permeabilized at room temperature with 0.1% TritonX for 15 minutes and blocked with 3% Bovine Serum Albumin (BSA) for 1h. Primary antibodies were incubated overnight in 3% BSA at 4 °C and secondary antibodies were incubated for 1-2h in 3% BSA at room temperature. Nuclei were labelled with Hoechst at 1:10,000 in PBS at room temperature for 15 min. Two 100 uL per well PBS washes were performed between each described step. All images were obtained using a 10x 0.4 numerical aperture objective on a Nikon TiE microscope.

4.5.5 Time-lapse microscopy

MCF10a cells were plated 24h prior to imaging and full growth media was replaced with phenol red-free full-growth media. Images were taken in CFP, YFP, and mCherry every 12 minutes at two sites per well that were spaced 2 mm apart. Total light exposure was kept below 600 ms. Cells were imaged in a humidified, 37°C chamber at 5% CO2. All images were obtained using a 10x 0.4 numerical aperture objective on a Nikon TiE microscope.

4.5.6 Image processing

Image processing and cell tracking were performed as previously described[118]. Phosho-Rb was separated into high and low modes by using the saddle-point in the data as the cutoff. Ki67off cells were classified as those less than the 95th percentile of the median nuclear signal in WT cells. Nuclear signals were quantified from a nuclear mask, which was generated using Otsu's method on cells stained for Hoechst. Cytoplasmic signals were quantified from a cytoplasmic mask, which was generated using Otsu's method on cells stained for succinimidyl ester. The regionprops function in MATLAB was used to quantify the mean signal for each stain from binary masks of the nucleus or cytoplasm. Immunofluorescence and SA-β-Gal signals were linked back to live-cell imaging traces by nearest neighbor screening after jitter correction as previously described[118].

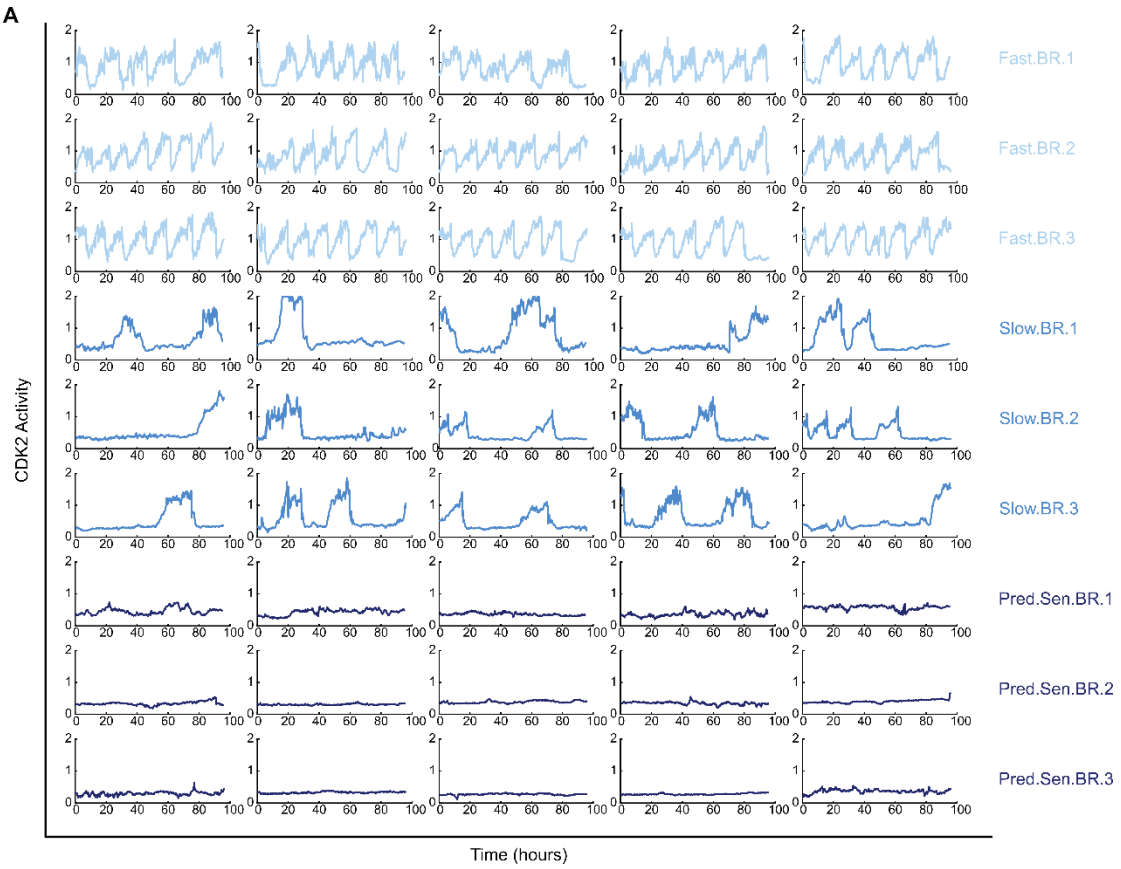
A
CDK2 Activity
Fast.BR.1
Fast.BR.2
Fast.BR.3
Slow.BR.1
Slow.BR.2
Slow.BR.3
Pred.Sen.BR.1
Pred.Sen.BR.2
Pred.Sen.BR.3
Time (hours)

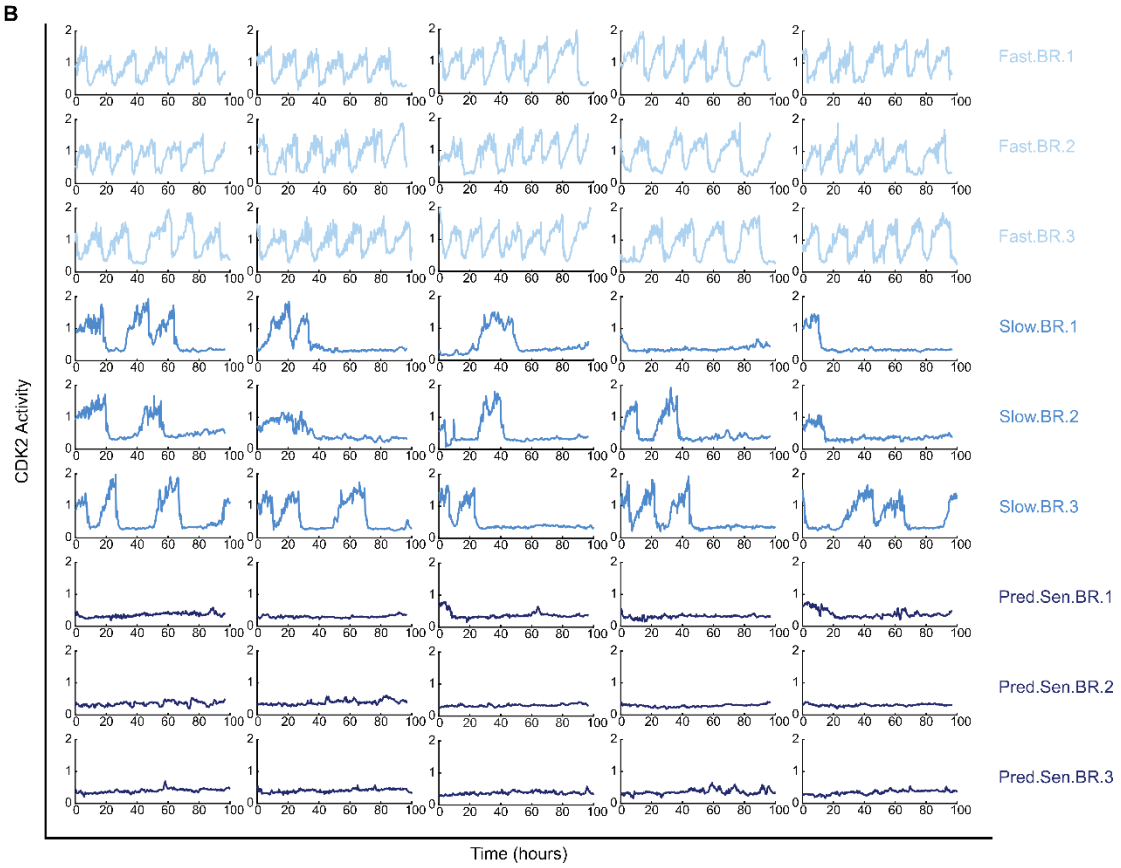
B
CDK2 Activity
Fast.BR.1
Fast.BR.2
Fast.BR.3
Slow.BR.1
Slow.BR.2
Slow.BR.3
Pred.Sen.BR.1
Pred.Sen.BR.2
Pred.Sen.BR.3
Time (hours)

Figure 4.1 Representative single-cell traces from multiple biological replicates for etoposide release (A-B) Five representative traces across three independent biological replicates (BRs) for fast-cycling, slow-cycling, and predicted-senescent categories following etoposide release (A) or hydrogen peroxide release (B).

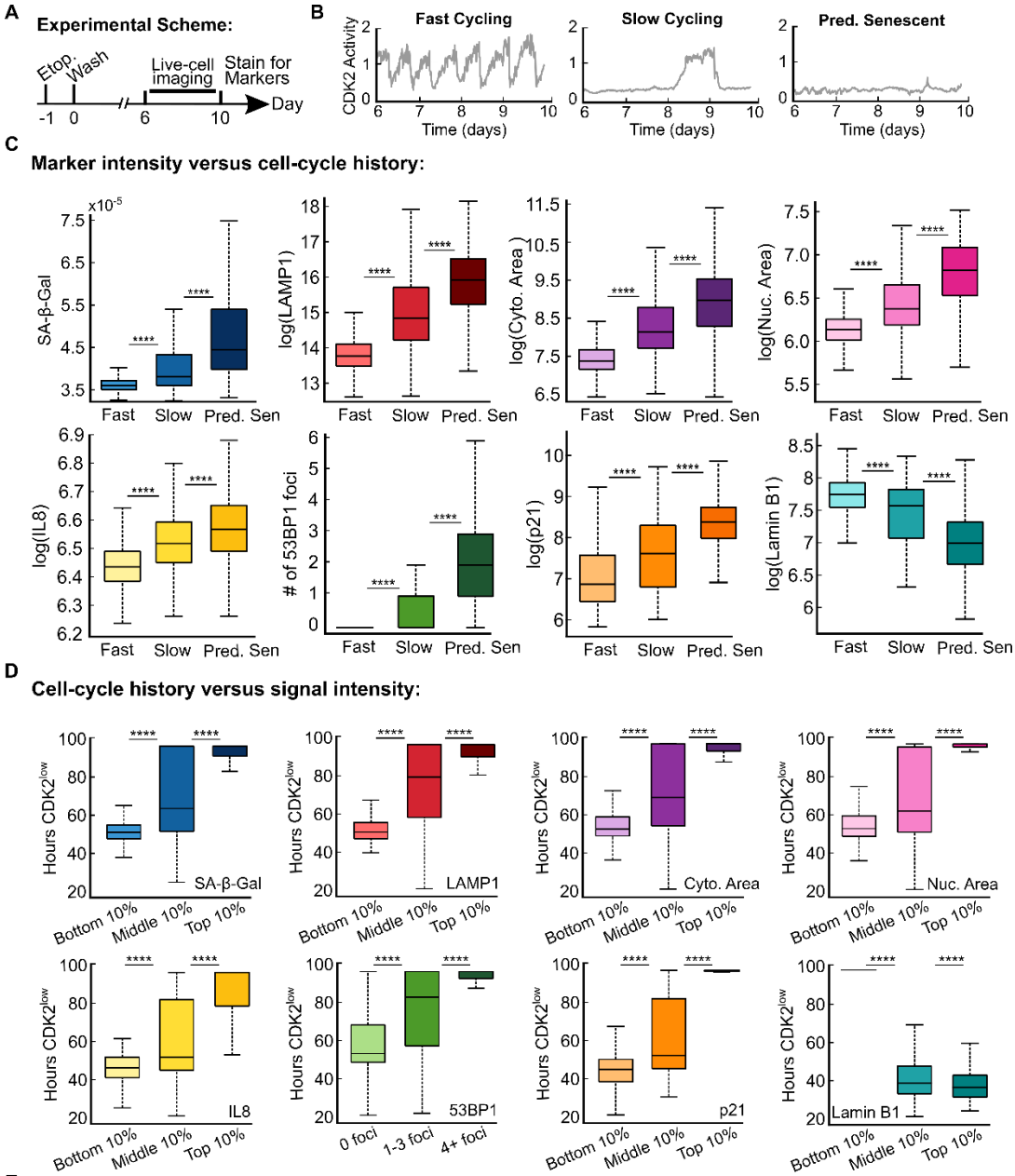
A
Experimental Scheme:
Etop.
Wash
Live-cell imaging
Stain for Markers
-1 0 6 10 Day
B
Fast Cycling
Slow Cycling
Pred. Senescent
CDK2 Activity
Time (days)
C
Marker intensity versus cell-cycle history:
SA-β-Gal
log(LAMP1)
log(Cyto. Area)
log(Nuc. Area)
log(IL8)
# of 53BP1 foci
log(p21)
log(Lamin B1)
Fast Slow Pred. Sen
D
Cell-cycle history versus signal intensity:
Hours CDK2low
SA-β-Gal
LAMP1
Cyto. Area
Nuc. Area
IL8
53BP1
p21
Lamin B1
Bottom 10% Middle 10% Top 10%
0 foci 1-3 foci 4+ foci
E
Receiver operating characteristic analysis
True Positive Rate
False Positive Rate
Whole population
Slow + Pred. Sen
Random
AUC = 0.77
AUC = 0.55
AUC = 0.80
AUC = 0.60
AUC = 0.77
AUC = 0.60
AUC = 0.78
AUC = 0.60
AUC = 0.79
AUC = 0.62
AUC = 0.73
AUC = 0.56
AUC = 0.87
AUC = 0.75
AUC = 0.89
AUC = 0.76

Figure 4.2 Senescence biomarkers resolve proliferating from non-proliferating cells better than slow-cycling from predicted-senescent cells (A-E) MCF10A cells expressing the CDK2 activity sensor were treated with 10 μM etoposide for 24h, washed, and subjected to time-lapse microscopy from 6d-10d after release. The cells were fixed and stained for SA-β-Gal, LAMP1, succinimidyl ester, Hoechst, IL8, 53BP1, p21, and Lamin B1 after the last frame was taken. (B-C) Cells were split into fast-cycling, slow-cycling, or predicted-senescent based on their duration spent $CDK2^{low}$ during live cell imaging, and the intensity of each marker was measured for each cellular fate. (D) The duration cells spent in the $CDK2^{low}$ state was plotted against the bottom, middle, and top 10% of signal for each marker. (E) ROC analysis for fast-cycling, slow-cycling, and predicted-senescent cells versus only slow-cycling and predicted-senescent cells. AUC indicates the area under the curve for each condition.

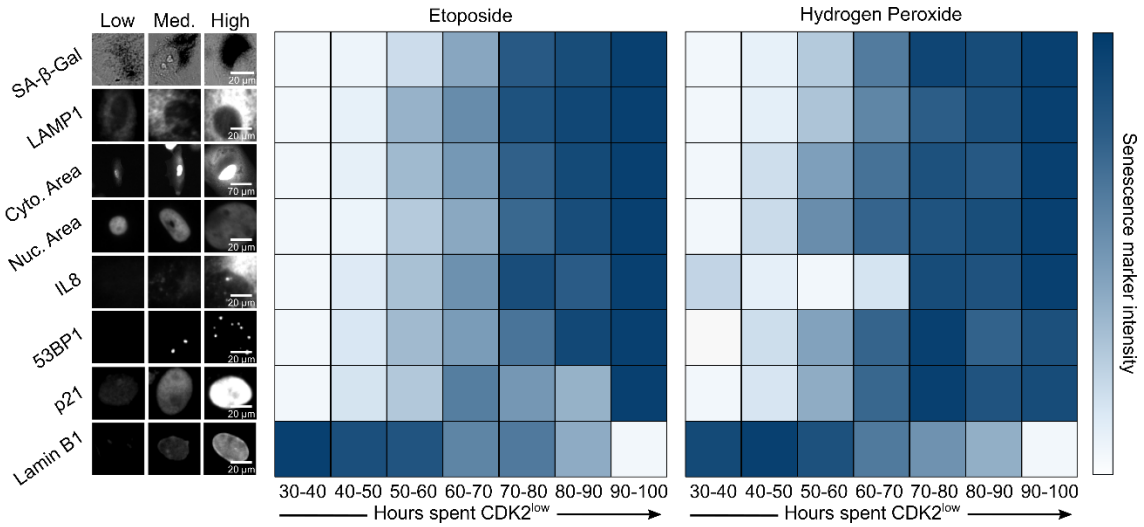

Figure 4.3. Cell-cycle withdrawal is graded rather than binary Cells were grouped based on the amount of time spent in the CDK2^{low} state. The Etoposide condition is data from Fig. 4.2. For the hydrogen peroxide condition, cells were treated for 2 hr with 100 μM H_2O_2 in OptiMEM before being washed twice and immediately filmed for 4 days. The marker intensities in each group were averaged, scaled between 0 and 1, and each box was colored accordingly. This reveals a gradual, monotonic accumulation of each marker signal as a function of the duration of cell-cycle withdrawal.

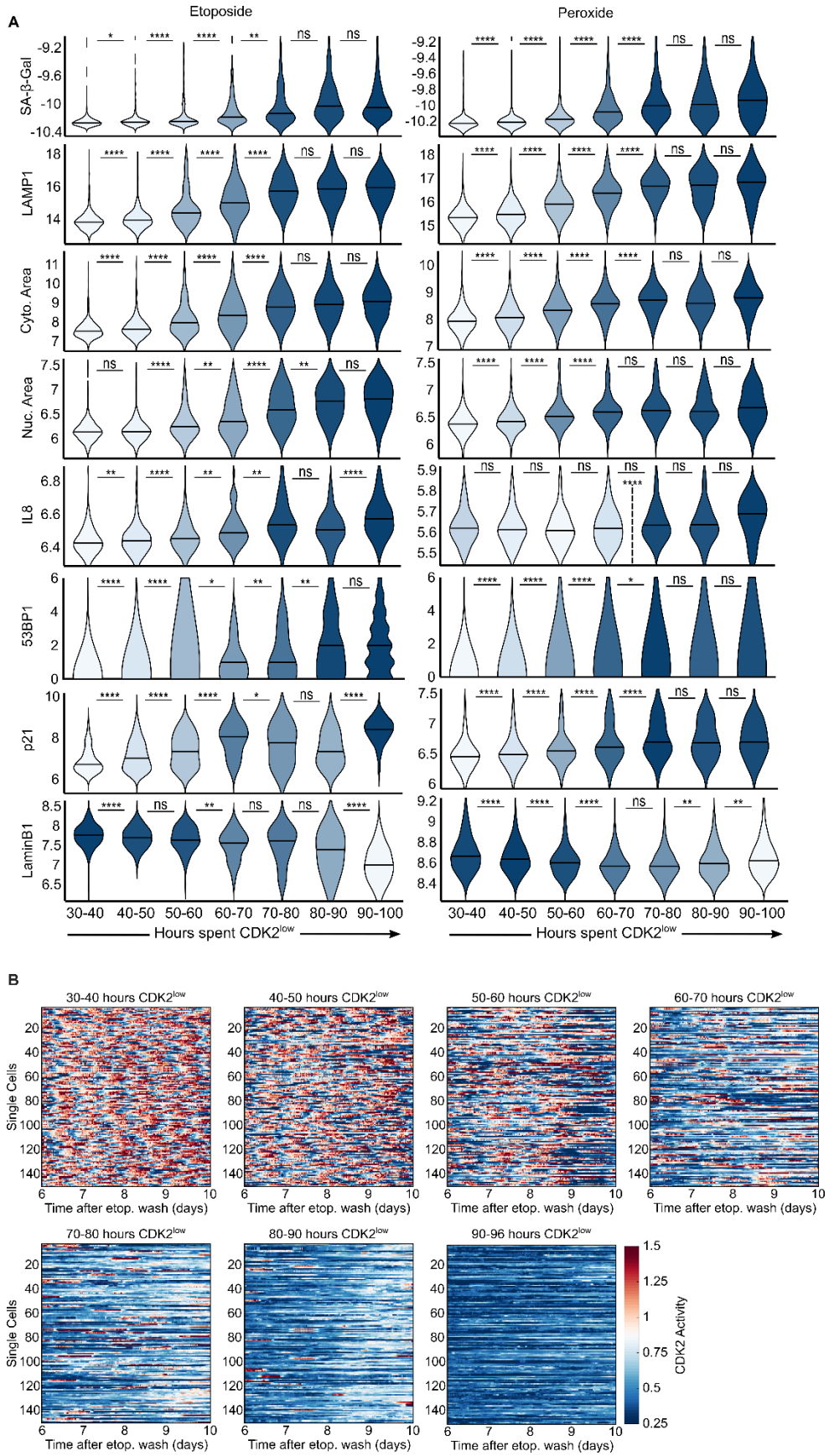
A
Etoposide
Peroxide
SA-β-Gal
LAMP1
Cyto. Area
Nuc. Area
IL8
53BP1
p21
LaminB1
30-40
40-50
50-60
60-70
70-80
80-90
90-100
Hours spent CDK2low
B
30-40 hours CDK2low
40-50 hours CDK2low
50-60 hours CDK2low
60-70 hours CDK2low
70-80 hours CDK2low
80-90 hours CDK2low
90-96 hours CDK2low
Single Cells
Time after etop. wash (days)
CDK2 Activity

Figure 4.4 Distributions of senescence marker intensity with respect to cell-cycle status (A) Violin plots of the data plotted in Figure 5. Black lines are the median of each distribution. An additional statistical test was performed on peroxide released cells stained for IL8 for cells that spent 30-70 hours $CDK2^{low}$ compared to cells that spent 70-96 hours $CDK2^{low}$, as indicated by the dashed line. (B) Heatmaps of 148 representative single-cell traces of CDK2 activity for each time bins specified in Fig. 4.4A.

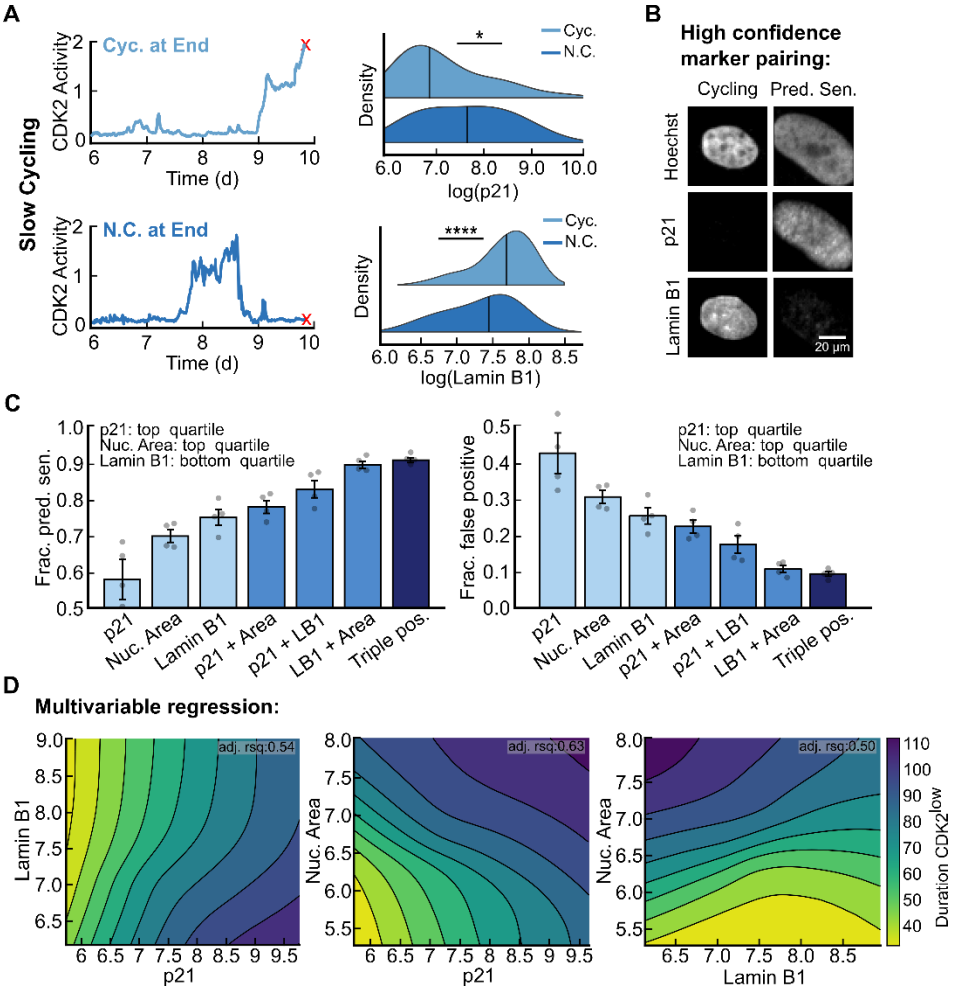

Figure 4.5. p21 and Lamin B1 are short-memory markers that resolve predicted senescent cells (A) Distributions of p21 and Lamin B1 in early versus late escaping subpopulations from the data in Fig. 4. (B) MCF10A cells were co-stained for Hoechst, p21, and Lamin B1 after being imaged from 6-10 days after a 24h treatment of 10 μM etoposide. The fraction of predicted-senescent cells and corresponding false positive rates were computed for every combination of markers using a binary cutoff at the top quartile of signal intensity. (C) Topological projections of local polynomial regression modeling of the data in Fig. 4.5B for each pair of senescence biomarkers with respect to the duration $CDK2^{low}$ during live-cell imaging.

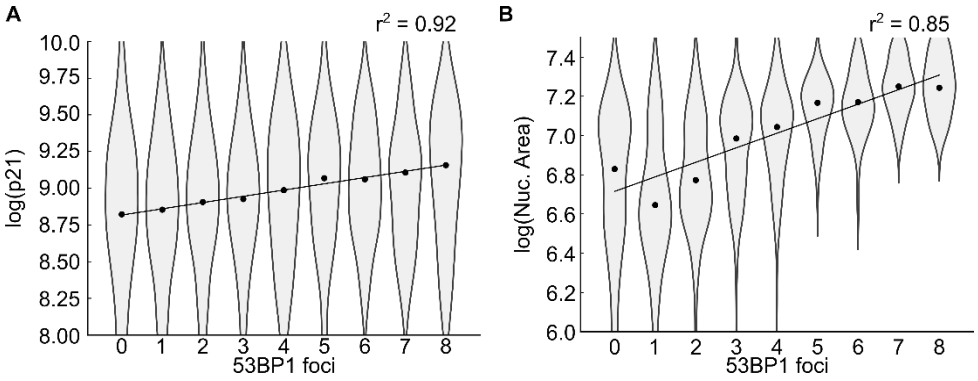

Figure 4.6. P21 and nuclear area binned by 53BP1 foci number (A-B) MCF10A cells were released for 6d from a 24h treatment of 10 μM etoposide and then fixed and stained for Hoechst, p21, and 53BP1. The distributions of (A) p21 and nuclear area (B) are plotted for increasing numbers of 53BP1 nuclear bodies. Black dots represent the mean of each distribution. The line is the line of best fit along the means.

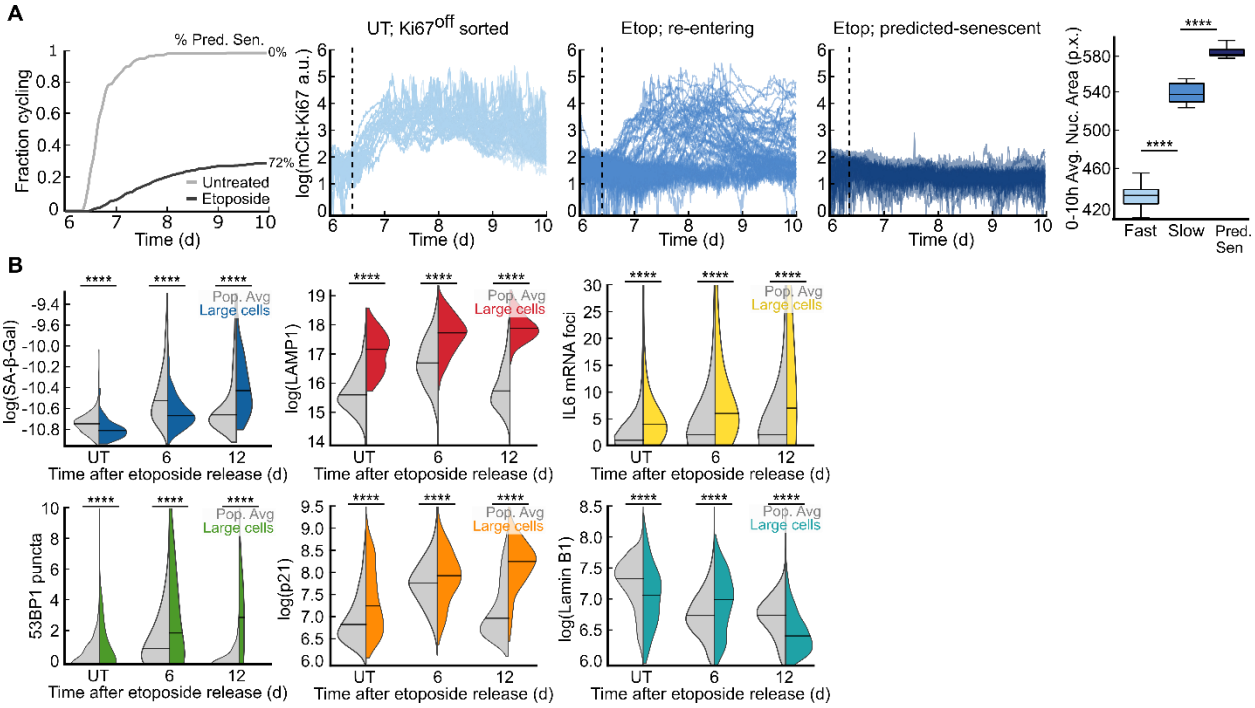

Figure 4.7. The largest cells in the population go on to accumulate features of truly senescent cells (A) The data as in Fig. 1.1E. Cumulative distribution function (CDF) curves represent the fraction of cells that re-enter the cell cycle during the movie; the remainder of cells are defined as senescent (72%). Cells were clustered based on their relative mCitrine-Ki67 signals: proliferating (untreated; gray); quiescent (etoposide released; blue); senescent (etoposide released; green). The mean nuclear area within the first 10h of filming was plotted for each category. SA-β-Gal, LAMP1, and IL6 mRNA, 53BP1, p21, and Lamin B1 signal were measured over the course of a 12d recovery after release from a 24h pulse of 10 μM etoposide treatment in all cells versus cells with cytoplasmic areas >95th percentile of UT cells.

Chapter 5

Discussion

5.1 Dissertation summary

The overarching goal of this thesis was to quantify and compare the cell-cycle withdrawal phenotypes that emerge in single cells following DNA-damaged induced senescence. To do this, we applied long-term single-cell timelapse microscopy followed by fixing and staining for several canonical senescence biomarkers. The studies and their major findings are summarized below:

(1) In this study, we explored the varying responses of cancer cells to chemotherapy utilizing live cell time-lapse microscopy to differentiate between cells that are reversibly arrested from those that are irreversibly arrested. We were able to link these distinct phenotypes to the extent of DNA damage and tumor suppressor signaling, demonstrating that senescence is induced incompletely in culture. Our findings highlight the heterogeneity of cancer cell responses to chemotherapy and the molecular mechanisms underlying reversibility in cell-cycle arrest.

(2) In this study, we developed a new method to quantify the senescence-associated-beta-galactosidase (SA-β-Gal) stain, a marker for senescent cells. We found that increased duration of cell-cycle exit is directly correlated with the intensity of SA-β-Gal staining and is present in slow-cycling, quiescent, and senescent cells. Our study also revealed that increased SA-β-Gal staining scales with increased lysosomal mass and autophagy in single cells. These data offer a more thorough understanding of SA-β-Gal positivity and its relationship to irreversible cell-cycle arrest and autophagy.

(3) In this study, we explored the use of multiple biomarkers to identify senescent cells more accurately. We quantified the intensity of staining of each marker with respect to cell-cycle status and compared the predictive power of these markers for classifying cells as senescent. These data suggest that the relative intensities of canonical senescence biomarkers encode information about the cell-cycle histories of single

cells released from acute DNA damage, suggesting that cell-cycle withdrawal exists on a continuum.

The projects described in this thesis provide new insights into the heterogeneity and complexity of cell-cycle withdrawal phenotypes following DNA damage-induced senescence. The studies highlight the importance of understanding the molecular mechanisms that drive senescence induction, and the critical role of tumor suppressor signaling in mediating senescence outcomes. Additionally, the findings suggest that senescence markers should be applied more quantitatively, as they encode meaningful information about cell-cycle history.

Overall, these studies contribute to our understanding of the heterogeneity of senescence outcomes in individual cells and offer new approaches for characterizing senescent cells. The insights gained from this work may have important implications for understanding the role of senescence in aging and age-related diseases, as well as for the development of novel therapeutic strategies targeting senescent cells.

5.2 SA-β-Gal staining and the causes and consequences of senescence

The SA-β-Gal stain is widely used to detect senescent cells, but our research has revealed new insights into its limitations and proposed more valuable alternatives. We have developed quantitative methods to measure SA-β-Gal staining and link it to cell-cycle history, which have led us to question its reliability as a marker for senescence. We have found that SA-β-Gal staining is graded and enriched across various types of cell-cycle exit and is strongly correlated with the duration of cell-cycle withdrawal. Additionally, we have observed a correlation between SA-β-Gal staining and an increase in lysosomal abundance, which reflects an increase in autophagic flux, a well-known feature of senescent cells[61,126]. While SA-β-Gal staining has been considered a reliable method for identifying senescent cells due to its apparently low background for other cellular states[119], we argue that this is only because the protocol is performed on fixed cells at suboptimal pH, which artificially reduces background staining.

Our findings suggest that measurements related to autophagy and lysosomal content may provide more valuable and quantitative information about the biology and dynamics of senescent cells than SA-β-Gal staining. One critical area of research is to understand how changes in autophagy are related to the reversibility of cell-cycle exit. Specifically, it remains unclear how to distinguish between increased total autophagic flux and decreased autophagic efficiency, and whether this is causal or consequential for irreversible cell-cycle arrest. Previous studies have suggested causal roles for decreased autophagic flux with increasing quiescence depth[128], but further investigation is needed to determine the underlying mechanisms of irreversible cell-cycle arrest, especially in the context of senescence induction. Recent work has identified that lysosomal proteins superscale with the proteome[137], indicating that increased autophagy in senescent cells may result from a loss of cell size control. However, follow-up research has suggested that the proteome content of cells is linked more to growth rate than to dysregulated cell size, and that markers that subscale/superscale with size but not growth rate may be critical regulators of the senescence phenotype[73].

While the consequences of senescence have been widely studied, such as SA-β-Gal staining, there is a growing need to understand the underlying causes of senescence, such as proteome scaling imbalance. The mechanisms that trigger cell-cycle arrest and the factors that contribute to the development of senescence are still not fully understood. Therefore, further investigation is required to gain insights into the molecular and cellular events that lead to senescence, and to identify potential targets for interventions that can delay or prevent the onset of age-related diseases. Understanding the causes of senescence is crucial to developing effective treatments for a variety of conditions associated with aging and will pave the way for more personalized and targeted therapies in the future.

5.3 Senescence markers and cell-cycle withdrawal are on a continuum

Quiescence is a state of reversible cell cycle arrest, while senescence denotes a state of irreversible cell cycle arrest. However, the classification of these states has primarily been based

on the expression of certain biomarkers, often unique to the specific stress conditions applied[25], rather than the cell-cycle exit phenotype, which has recently been shown to be heterogenous in nature. As a result, there has been limited exploration of whether quiescent and senescent cells co-exist within the same population or whether these states uniquely emerge in response to distinct cellular stresses. Moreover, because reversible and irreversible cell-cycle withdrawal are defined by a set of overlapping molecular markers, it is unclear whether these states are truly distinct on a single-cell level[104]. Our work and that of others have challenged the conventional distinction between quiescence and senescence. For example, Fujimaki et al. (2019) demonstrated that serum starvation-induced quiescence leads to a continuum of senescent-like gene expression changes, suggesting the existence of multiple depths of cell-cycle exit[128]. Similarly, Stallaert et al. (2022) revealed a continuum of markers of cell-cycle exit, with unique arrest trajectories induced by diverse stressors[32]. Our own research indicates that reversible and irreversible cell-cycle exit cannot be easily distinguished by biomarker staining, and that the staining intensity is a critical determinant of the likelihood of re-entry into the cell cycle.

Furthermore, we and others found that cell-cycle heterogeneity in the response to DNA damage stress is linked to p53-p21 signaling, where the severity and duration of stress dictates future proliferative capacity. Collectively, these observations point towards a continuum model for cell-cycle exit, where quiescence and senescence represent different points along the spectrum of cell-cycle withdrawal, rather than entirely distinct states.

The graded relationship between marker intensity and cell-cycle withdrawal duration is perhaps unsurprising due to the interconnected nature of the signaling pathways that drive cellular senescence. Increased levels of DNA damage drive increased expression of p21 [139,140], which inhibits CDK2 activity to halt cell-cycle progression [11,123]. This blockade in proliferation causes a transcriptional decline in E2F targets such as Lamin B1 [141], which is also a substrate for selective autophagy in senescent cells[142]. Furthermore, increased lysosomal content (E.g., SA-β-Gal and LAMP1) and upregulation of the SASP (E.g., IL8 and IL6) are both linked to DNA-damage

response signaling [61,74,143] as well as imbalanced proteome scaling from increased cell size [73,97,137,138], a recently reported causal feature of senescence induction. As a result, we postulate that the molecular features associated with senescent cells are primarily caused by 1) DNA-damage-induced tumor suppressor signaling and 2) dysregulated cell size scaling, and the intensities of these signals are directly reflective of the level of stress experienced by the cell.

Understanding the molecular mechanisms that underlie these transitions could shed light on the complex interplay between stress response pathways and cell-cycle commitment. This research may ultimately have important implications for the development of therapeutic interventions that target senescence-associated diseases as well as cancer. If stress-induced quiescence and senescence represent different degrees of cell-cycle withdrawal along a continuum rather than entirely distinct states, it is critical to determine whether there is a point of no return for cell-cycle re-entry or if the likelihood of re-entry decreases steadily as cells progress along this continuum. Furthermore, this model suggests that it may be feasible to induce deeply quiescent cells to re-enter the cell cycle to promote tissue rejuvenation or drive quiescent cancer cells towards senescence to prevent tumor recurrence. Our work demonstrates that snapshot data encodes dynamic information about the past, which can be extrapolated to predict cellular behavior in the future. By devising strategies to retrieve such information, we can uncover new temporal control mechanisms that govern cellular behavior in vivo. This could aid in the interpretation of pathology staining and provide important clinical benefits by enabling clinicians to infer both past and future cellular behavior from fixed tissue samples.

5.4 Future Directions

While the work presented in this thesis will be useful for the cell cycle and senescence fields, there are important future directions about the unambiguous classification of senescent cells. Our work suggests that no single marker offers sufficient resolution to classify cells as senescent versus quiescent, calling into question the importance of distinguishing these cellular states from a biological standpoint. However, we only quantified a handful of markers associated

with senescent cells. Using single-cell RNA sequencing, we plan to confirm our model by comparing the transcriptomic signatures of cells that are reversibly versus irreversibly arrested at multiple timepoints.

Additionally, we plan to evaluate several senescence features using 4i/ CyCIF[32,40] to create a senescence score that we may translate to a clinical context given access to patient samples. In this case, we could determine whether quantitative measures of senescence correlate with patient outcomes in a variety of drug on/off contexts. This would help inform which types of cancers and treatments senescence is therapeutically beneficial vs. detrimental.

Bibliography

1. Harper, J. V. & Brooks, G. The Mammalian Cell Cycle. in *Cell Cycle Control: Mechanisms and Protocols* (eds. Humphrey, T. & Brooks, G.) 113–153 (Humana Press, 2005). doi:10.1385/1-59259-857-9:113.
2. Gookin, S. *et al.* A map of protein dynamics during cell-cycle progression and cell-cycle exit. *PLOS Biol.* **15**, e2003268 (2017).
3. Dhillon, A. S., Hagan, S., Rath, O. & Kolch, W. MAP kinase signalling pathways in cancer. *Oncogene* **26**, 3279–3290 (2007).
4. Hanahan, D. & Weinberg, R. A. Hallmarks of Cancer: The Next Generation. *Cell* **144**, 646–674 (2011).
5. Braicu, C. *et al.* A Comprehensive Review on MAPK: A Promising Therapeutic Target in Cancer. *Cancers* **11**, 1618 (2019).
6. Guo, Y.-J. *et al.* ERK/MAPK signalling pathway and tumorigenesis (Review). *Exp. Ther. Med.* **19**, 1997–2007 (2020).
7. Chung, M. *et al.* Transient Hysteresis in CDK4/6 Activity Underlies Passage of the Restriction Point in G1. *Mol. Cell* **76**, 562-573.e4 (2019).
8. Hatakeyama, M. & Weinberg, R. A. The role of RB in cell cycle control. *Prog. Cell Cycle Res.* **1**, 9–19 (1995).
9. Liu, C. *et al.* Altered G1 signaling order and commitment point in cells proliferating without CDK4/6 activity. *Nat. Commun.* **11**, 5305 (2020).
10. Yang, H. W. *et al.* Stress-mediated exit to quiescence restricted by increasing persistence in CDK4/6 activation. *eLife* **9**, e44571 (2020).
11. Moser, J., Miller, I., Carter, D. & Spencer, S. L. Control of the Restriction Point by Rb and p21. *Proc. Natl. Acad. Sci. U. S. A.* **115**, E8219–E8227 (2018).
12. Spencer, S. L. *et al.* The Proliferation-Quiescence Decision Is Controlled by a Bifurcation in CDK2 Activity at Mitotic Exit. *Cell* **155**, 369–383 (2013).
13. Narasimha, A. M. *et al.* Cyclin D activates the Rb tumor suppressor by mono-phosphorylation. *eLife* **3**, e02872 (2014).
14. Rubin, S. M. Deciphering the Rb phosphorylation code. *Trends Biochem. Sci.* **38**, 12–19 (2013).
15. Yao, G., Lee, T. J., Mori, S., Nevins, J. R. & You, L. A bistable Rb–E2F switch underlies the restriction point. *Nat. Cell Biol.* **10**, 476–482 (2008).
16. Donjerkovic, D. & Scott, D. W. Regulation of the G1 phase of the mammalian cell cycle. *Cell Res.* **10**, 1–16 (2000).
17. Mei, L. & Cook, J. G. Efficiency and equity in origin licensing to ensure complete DNA replication. *Biochem. Soc. Trans.* **49**, 2133–2141 (2021).
18. Bartek, J., Lukas, C. & Lukas, J. Checking on DNA damage in S phase. *Nat. Rev. Mol. Cell Biol.* **5**, 792–804 (2004).
19. Stark, G. R. & Taylor, W. R. Analyzing the G2/M Checkpoint. in *Checkpoint Controls and Cancer: Volume 1: Reviews and Model Systems* (ed. Schönthal, A. H.) 51–82 (Humana Press, 2004). doi:10.1385/1-59259-788-2:051.
20. McIntosh, J. R. Mitosis. *Cold Spring Harb. Perspect. Biol.* **8**, a023218 (2016).
21. Swaffer, M. P., Jones, A. W., Flynn, H. R., Snijders, A. P. & Nurse, P. CDK Substrate Phosphorylation and Ordering the Cell Cycle. *Cell* **167**, 1750-1761.e16 (2016).
22. Nakayama, K. I. & Nakayama, K. Ubiquitin ligases: cell-cycle control and cancer. *Nat. Rev. Cancer* **6**, 369–381 (2006).
23. Teixeira, L. K. & Reed, S. I. Ubiquitin Ligases and Cell Cycle Control. *Annu. Rev. Biochem.* **82**, 387–414 (2013).

24. Cheung, T. H. & Rando, T. A. Molecular regulation of stem cell quiescence. *Nat. Rev. Mol. Cell Biol.* **14**, 329–340 (2013).
25. Marescal, O. & Cheeseman, I. M. Cellular Mechanisms and Regulation of Quiescence. *Dev. Cell* **55**, 259–271 (2020).
26. Cheshier, S. H., Morrison, S. J., Liao, X. & Weissman, I. L. In vivo proliferation and cell cycle kinetics of long-term self-renewing hematopoietic stem cells. *Proc. Natl. Acad. Sci.* **96**, 3120–3125 (1999).
27. Hümmer, J., Kraus, S., Brändle, K. & Lee-Thedieck, C. Nitric Oxide in the Control of the in vitro Proliferation and Differentiation of Human Hematopoietic Stem and Progenitor Cells. *Front. Cell Dev. Biol.* **8**, (2021).
28. Zetterberg, A. & Larsson, O. Coordination between Cell Growth and Cell Cycle Transit in Animal Cells. *Cold Spring Harb. Symp. Quant. Biol.* **56**, 137–147 (1991).
29. van Velthoven, C. T. J. & Rando, T. A. Stem Cell Quiescence: Dynamism, Restraint, and Cellular Idling. *Cell Stem Cell* **24**, 213–225 (2019).
30. Yao, G. Modelling mammalian cellular quiescence. *Interface Focus* **4**, 20130074 (2014).
31. Min, M. & Spencer, S. L. Spontaneously slow-cycling subpopulations of human cells originate from activation of stress-response pathways. *PLOS Biol.* **17**, e3000178 (2019).
32. Stallaert, W. *et al.* The molecular architecture of cell cycle arrest. *Mol. Syst. Biol.* **18**, e11087 (2022).
33. Fan, Y. & Meyer, T. Molecular control of cell density-mediated exit to quiescence. *Cell Rep.* **36**, 109436 (2021).
34. Crozier, L. *et al.* CDK4/6 inhibitors induce replication stress to cause long-term cell cycle withdrawal. *EMBO J.* **41**, e108599 (2022).
35. Pennycook, B. R. & Barr, A. R. Palbociclib-mediated cell cycle arrest can occur in the absence of the CDK inhibitors p21 and p27. *Open Biol.* **11**, 210125 (2022).
36. Arora, M., Moser, J., Phadke, H., Basha, A. A. & Spencer, S. L. Endogenous Replication Stress in Mother Cells Leads to Quiescence of Daughter Cells. *Cell Rep.* **19**, 1351–1364 (2017).
37. Panier, S. & Boulton, S. J. Double-strand break repair: 53BP1 comes into focus. *Nat. Rev. Mol. Cell Biol.* **15**, 7–18 (2014).
38. Abukhdeir, A. M. & Park, B. H. p21 and p27. *Expert Rev. Mol. Med.* **10**, e19 (2008).
39. Coqueret, O. New roles for p21 and p27 cell-cycle inhibitors: a function for each cell compartment? *Trends Cell Biol.* **13**, 65–70 (2003).
40. Stallaert, W. *et al.* The structure of the human cell cycle. *Cell Syst.* **13**, 230-240.e3 (2022).
41. Engeland, K. Cell cycle regulation: p53-p21-RB signaling. *Cell Death Differ.* **29**, 946–960 (2022).
42. Sharpless, N. E. & Sherr, C. J. Forging a signature of in vivo senescence. *Nat. Rev. Cancer* **15**, 397–408 (2015).
43. Lange, T. de. Shelterin: the protein complex that shapes and safeguards human telomeres. *Genes Dev.* **19**, 2100–2110 (2005).
44. Vaiserman, A. & Krasnienkov, D. Telomere Length as a Marker of Biological Age: State-of-the-Art, Open Issues, and Future Perspectives. *Front. Genet.* **11**, (2021).
45. Nassrally, M. S. *et al.* Cell cycle arrest in replicative senescence is not an immediate consequence of telomere dysfunction. *Mech. Ageing Dev.* **179**, 11–22 (2019).
46. López-Otín, C., Blasco, M. A., Partridge, L., Serrano, M. & Kroemer, G. The Hallmarks of Aging. *Cell* **153**, 1194–1217 (2013).
47. Coppé, J.-P., Desprez, P.-Y., Krtolica, A. & Campisi, J. The senescence-associated secretory phenotype: the dark side of tumor suppression. *Annu. Rev. Pathol.* **5**, 99–118 (2010).
48. Coppé, J.-P. *et al.* Senescence-Associated Secretory Phenotypes Reveal Cell-Nonautonomous Functions of Oncogenic RAS and the p53 Tumor Suppressor. *PLOS Biol.* **6**, e301 (2008).

49. Baker, D. J. *et al.* Clearance of p16Ink4a-positive senescent cells delays ageing-associated disorders. *Nature* **479**, 232–236 (2011).
50. Chang, J. *et al.* Clearance of senescent cells by ABT263 rejuvenates aged hematopoietic stem cells in mice. *Nat. Med.* **22**, 78–83 (2016).
51. Beauséjour, C. M. *et al.* Reversal of human cellular senescence: roles of the p53 and p16 pathways. *EMBO J.* **22**, 4212–4222 (2003).
52. Ruscetti, M. *et al.* NK cell–mediated cytotoxicity contributes to tumor control by a cytostatic drug combination. *Science* **362**, 1416–1422 (2018).
53. Bousset, L. & Gil, J. Targeting senescence as an anticancer therapy. *Mol. Oncol.* **16**, 3855–3880 (2022).
54. McHugh, D. & Gil, J. Senescence and aging: Causes, consequences, and therapeutic avenues. *J. Cell Biol.* **217**, 65–77 (2018).
55. Aubrey, B. J., Kelly, G. L., Janic, A., Herold, M. J. & Strasser, A. How does p53 induce apoptosis and how does this relate to p53-mediated tumour suppression? *Cell Death Differ.* **25**, 104–113 (2018).
56. Liu, J.-Y. *et al.* Cells exhibiting strong p16INK4a promoter activation in vivo display features of senescence. *Proc. Natl. Acad. Sci.* **116**, 2603–2611 (2019).
57. Rayess, H., Wang, M. B. & Srivatsan, E. S. Cellular senescence and tumor suppressor gene p16. *Int. J. Cancer J. Int. Cancer* **130**, 1715–1725 (2012).
58. Krishnamurthy, J. *et al.* Ink4a/Arf expression is a biomarker of aging. *J. Clin. Invest.* **114**, 1299–1307 (2004).
59. Liu, Y. *et al.* Expression of p16INK4a in peripheral blood T-cells is a biomarker of human aging. *Aging Cell* **8**, 439–448 (2009).
60. Dimri, G. P. *et al.* A biomarker that identifies senescent human cells in culture and in aging skin in vivo. *Proc. Natl. Acad. Sci. U. S. A.* **92**, 9363–9367 (1995).
61. Kurz, D. J., Decary, S., Hong, Y. & Erusalimsky, J. D. Senescence-associated (beta)-galactosidase reflects an increase in lysosomal mass during replicative ageing of human endothelial cells. *J. Cell Sci.* **113**, 3613–3622 (2000).
62. Lee, B. Y. *et al.* Senescence-associated β-galactosidase is lysosomal β-galactosidase. *Aging Cell* **5**, 187–195 (2006).
63. Mauthe, M. *et al.* Chloroquine inhibits autophagic flux by decreasing autophagosome-lysosome fusion. *Autophagy* **14**, 1435–1455 (2018).
64. Gary, R. K. & Kindell, S. M. Quantitative assay of senescence-associated β-galactosidase activity in mammalian cell extracts. *Anal. Biochem.* **343**, 329–334 (2005).
65. González-Gualda, E., Baker, A. G., Fruk, L. & Muñoz-Espín, D. A guide to assessing cellular senescence in vitro and in vivo. *FEBS J.* **288**, 56–80 (2021).
66. Xie, S., Swaffer, M. & Skotheim, J. M. Eukaryotic Cell Size Control and Its Relation to Biosynthesis and Senescence. *Annu. Rev. Cell Dev. Biol.* **38**, 291–319 (2022).
67. Zhu, J. & Thompson, C. B. Metabolic regulation of cell growth and proliferation. *Nat. Rev. Mol. Cell Biol.* **20**, 436–450 (2019).
68. Mayer, C. & Grummt, I. Ribosome biogenesis and cell growth: mTOR coordinates transcription by all three classes of nuclear RNA polymerases. *Oncogene* **25**, 6384–6391 (2006).
69. Wiley, C. D. & Campisi, J. The metabolic roots of senescence: mechanisms and opportunities for intervention. *Nat. Metab.* **3**, 1290–1301 (2021).
70. Lanz, M. C. *et al.* Increasing cell size remodels the proteome and promotes senescence. *Mol. Cell* **82**, 3255-3269.e8 (2022).
71. Neurohr, G. E. & Amon, A. Relevance and regulation of cell density. *Trends Cell Biol.* **30**, 213–225 (2020).

72. Neurohr, G. E. *et al.* Excessive Cell Growth Causes Cytoplasm Dilution And Contributes to Senescence. *Cell* **176**, 1083-1097.e18 (2019).
73. Zatulovskiy, E. *et al.* Delineation of proteome changes driven by cell size and growth rate. *Front. Cell Dev. Biol.* **10**, 980721 (2022).
74. Kang, C. *et al.* The DNA damage response induces inflammation and senescence by inhibiting autophagy of GATA4. *Science* **349**, aaa5612 (2015).
75. Amor, C. *et al.* Senolytic CAR T cells reverse senescence-associated pathologies. *Nature* **583**, 127–132 (2020).
76. Freund, A., Laberge, R.-M., Demaria, M. & Campisi, J. Lamin B1 loss is a senescence-associated biomarker. *Mol. Biol. Cell* **23**, 2066–2075 (2012).
77. Kosar, M. *et al.* Senescence-associated heterochromatin foci are dispensable for cellular senescence, occur in a cell type- and insult-dependent manner and follow expression of p16ink4a. *Cell Cycle* **10**, 457–468 (2011).
78. Zhang, R., Chen, W. & Adams, P. D. Molecular Dissection of Formation of Senescence-Associated Heterochromatin Foci. *Mol. Cell. Biol.* **27**, 2343–2358 (2007).
79. Yosef, R. *et al.* Directed elimination of senescent cells by inhibition of BCL-W and BCL-XL. *Nat. Commun.* **7**, 11190 (2016).
80. Wiley, C. D. *et al.* Mitochondrial Dysfunction Induces Senescence with a Distinct Secretory Phenotype. *Cell Metab.* **23**, 303–314 (2016).
81. Kang, C. & Elledge, S. J. How autophagy both activates and inhibits cellular senescence. *Autophagy* **12**, 898–899 (2016).
82. Kirschner, K., Rattanavirotkul, N., Quince, M. F. & Chandra, T. Functional heterogeneity in senescence. *Biochem. Soc. Trans.* **48**, 765–773 (2020).
83. Cohn, R. L., Gasek, N. S., Kuchel, G. A. & Xu, M. The heterogeneity of cellular senescence: insights at the single-cell level. *Trends Cell Biol.* **33**, 9–17 (2023).
84. Moiseeva, V. *et al.* Context-dependent roles of cellular senescence in normal, aged, and disease states. *FEBS J.* **290**, 1161–1185 (2023).
85. Hsu, C.-H., Altschuler, S. J. & Wu, L. F. Patterns of Early p21 Dynamics Determine Proliferation-Senescence Cell Fate after Chemotherapy. *Cell* **178**, 361-373.e12 (2019).
86. Skipper, H. & Brockman, W. Implications of biochemical cytokinetic pharmacologic and toxicologic relationships in the design of optimal therapeutic schedules. *Cancer Chemother. Rep.* **54**, 431–450 (1970).
87. Moore, N., Houghton, J. & Lyle, S. Slow-Cycling Therapy-Resistant Cancer Cells. *Stem Cells Dev.* **21**, 1822–1830 (2012).
88. Reyes, J. *et al.* Fluctuations in p53 signaling allow escape from cell cycle arrest. *Mol. Cell* **71**, 581-591.e5 (2018).
89. Mansoori, B., Mohammadi, A., Davudian, S., Shirjang, S. & Baradaran, B. The Different Mechanisms of Cancer Drug Resistance: A Brief Review. *Adv. Pharm. Bull.* **7**, 339–348 (2017).
90. Wang, L., Lankhorst, L. & Bernards, R. Exploiting senescence for the treatment of cancer. *Nat. Rev. Cancer* **22**, 340–355 (2022).
91. Fujimaki, K. *et al.* Graded regulation of cellular quiescence depth between proliferation and senescence by a lysosomal dimmer switch. *Proc. Natl. Acad. Sci.* **116**, 22624–22634 (2019).
92. Fujimaki, K. & Yao, G. Cell dormancy plasticity: quiescence deepens into senescence through a dimmer switch. *Physiol. Genomics* **52**, 558–562 (2020).
93. Kwon, J. S. *et al.* Controlling Depth of Cellular Quiescence by an Rb-E2F Network Switch. *Cell Rep.* **20**, 3223–3235 (2017).
94. Miller, I. *et al.* Ki67 is a Graded Rather than a Binary Marker of Proliferation versus Quiescence. *Cell Rep.* **24**, 1105-1112.e5 (2018).

95. Marthandan, S., Priebe, S., Hemmerich, P., Klement, K. & Diekmann, S. Long-Term Quiescent Fibroblast Cells Transit into Senescence. *PLoS ONE* **9**, e115597 (2014).
96. Ezgi Wood, N., Kositangool, P., Hariri, H., Marchand, A. J. & Mike Henne, W. Nutrient Signaling, Stress Response, and Inter-organelle Communication Are Non-canonical Determinants of Cell Fate. *Cell Rep.* **33**, 108446 (2020).
97. Lengefeld, J. *et al.* Cell size is a determinant of stem cell potential during aging. *Sci. Adv.* **7**, eabk0271 (2021).
98. Cappell, S. D., Chung, M., Jaimovich, A., Spencer, S. L. & Meyer, T. Irreversible APCCdh1 Inactivation Underlies the Point of No Return for Cell-Cycle Entry. *Cell* **166**, 167–180 (2016).
99. Tian, C., Yang, C. & Spencer, S. L. EllipTrack: A Global-Local Cell-Tracking Pipeline for 2D Fluorescence Time-Lapse Microscopy. *Cell Rep.* **32**, 107984 (2020).
100. Inwald, E. C. *et al.* Ki-67 is a prognostic parameter in breast cancer patients: results of a large population-based cohort of a cancer registry. *Breast Cancer Res. Treat.* **139**, 539–552 (2013).
101. Wu, Q. *et al.* Prognostic Value of Ki-67 in Patients With Resected Triple-Negative Breast Cancer: A Meta-Analysis. *Front. Oncol.* **9**, (2019).
102. Barr, A. R. *et al.* DNA damage during S-phase mediates the proliferation-quiescence decision in the subsequent G1 via p21 expression. *Nat. Commun.* **8**, 14728 (2017).
103. Daigh, L. H., Liu, C., Chung, M., Cimprich, K. A. & Meyer, T. Stochastic Endogenous Replication Stress Causes ATR-Triggered Fluctuations in CDK2 Activity that Dynamically Adjust Global DNA Synthesis Rates. *Cell Syst.* **7**, 17-27.e3 (2018).
104. Pack, L. R., Daigh, L. H. & Meyer, T. Putting the brakes on the cell cycle: mechanisms of cellular growth arrest. *Curr. Opin. Cell Biol.* **60**, 106–113 (2019).
105. Ryl, T. *et al.* Cell-Cycle Position of Single MYC-Driven Cancer Cells Dictates Their Susceptibility to a Chemotherapeutic Drug. *Cell Syst.* **5**, 237-250.e8 (2017).
106. Maya-Mendoza, A. *et al.* Immortalised breast epithelia survive prolonged DNA replication stress and return to cycle from a senescent-like state. *Cell Death Dis.* **5**, e1351–e1351 (2014).
107. Milanovic, M. *et al.* Senescence-associated reprogramming promotes cancer stemness. *Nature* **553**, 96–100 (2018).
108. Hsu, C.-H., Altschuler, S. J. & Wu, L. F. Patterns of Early p21 Dynamics Determine Proliferation-Senescence Cell Fate after Chemotherapy. *Cell* **178**, 361-373.e12 (2019).
109. Reyes, J. *et al.* Fluctuations in p53 Signaling Allow Escape from Cell-Cycle Arrest. *Mol. Cell* **71**, 581-591.e5 (2018).
110. Lindell, E., Zhong, L. & Zhang, X. Quiescent Cancer Cells—A Potential Therapeutic Target to Overcome Tumor Resistance and Relapse. *Int. J. Mol. Sci.* **24**, 3762 (2023).
111. Chen, K. *et al.* The metabolic flexibility of quiescent CSC: implications for chemotherapy resistance. *Cell Death Dis.* **12**, 1–12 (2021).
112. Bruschini, S., Ciliberto, G. & Mancini, R. The emerging role of cancer cell plasticity and cell-cycle quiescence in immune escape. *Cell Death Dis.* **11**, 1–3 (2020).
113. Baldwin, E. L. & Osheroff, N. Etoposide, topoisomerase II and cancer. *Curr. Med. Chem. Anti-Cancer Agents* **5**, 363–372 (2005).
114. Miller, I. *et al.* Ki67 is a Graded Rather than a Binary Marker of Proliferation versus Quiescence. *Cell Rep.* **24**, 1105-1112.e5 (2018).
115. d'Adda di Fagagna, F. Living on a break: cellular senescence as a DNA-damage response. *Nat. Rev. Cancer* **8**, 512–522 (2008).
116. Arora, M., Moser, J., Phadke, H., Basha, A. A. & Spencer, S. L. Endogenous Replication Stress in Mother Cells Leads to Quiescence of Daughter Cells. *Cell Rep.* **19**, 1351–1364 (2017).

117. Saleh, T., Tyutyunyk-Massey, L. & Gewirtz, D. A. Tumor Cell Escape from Therapy-Induced Senescence as a Model of Disease Recurrence after Dormancy. *Cancer Res.* **79**, 1044–1046 (2019).
118. Gookin, S. *et al.* A map of protein dynamics during cell-cycle progression and cell-cycle exit. *PLOS Biol.* **15**, e2003268 (2017).
119. Dimri, G. P. *et al.* A biomarker that identifies senescent human cells in culture and in aging skin in vivo. *Proc. Natl. Acad. Sci.* **92**, 9363–9367 (1995).
120. Sharpless, N. E. & Sherr, C. J. Forging a signature of in vivo senescence. *Nat. Rev. Cancer* **15**, 397–408 (2015).
121. Lee, B. Y. *et al.* Senescence-associated β-galactosidase is lysosomal β-galactosidase. *Aging Cell* **5**, 187–195 (2006).
122. Hatakeyama, M. & Weinberg, R. A. The role of RB in cell cycle control. *Prog. Cell Cycle Res.* **1**, 9–19 (1995).
123. Spencer, S. L. *et al.* The Proliferation-Quiescence Decision Is Controlled by a Bifurcation in CDK2 Activity at Mitotic Exit. *Cell* **155**, 369–383 (2013).
124. Min, M. & Spencer, S. L. Spontaneously slow-cycling subpopulations of human cells originate from activation of stress-response pathways. *PLOS Biol.* **17**, e3000178 (2019).
125. Kurz, D. J., Decary, S., Hong, Y. & Erusalimsky, J. D. Senescence-associated β-galactosidase reflects an increase in lysosomal mass during replicative ageing of human endothelial cells. 10.
126. Kang, C. & Elledge, S. J. How autophagy both activates and inhibits cellular senescence. *Autophagy* **12**, 898–899 (2016).
127. Mauthe, M. *et al.* Chloroquine inhibits autophagic flux by decreasing autophagosome-lysosome fusion. *Autophagy* **14**, 1435–1455 (2018).
128. Fujimaki, K. *et al.* Graded regulation of cellular quiescence depth between proliferation and senescence by a lysosomal dimmer switch. *Proc. Natl. Acad. Sci.* **116**, 22624–22634 (2019).
129. Kirkland, J. L. & Tchkonia, T. Senolytic drugs: from discovery to translation. *J. Intern. Med.* **288**, 518–536 (2020).
130. Gasek, N. S., Kuchel, G. A., Kirkland, J. L. & Xu, M. Strategies for targeting senescent cells in human disease. *Nat. Aging* **1**, 870–879 (2021).
131. Rodier, F. & Campisi, J. Four faces of cellular senescence. *J. Cell Biol.* **192**, 547–556 (2011).
132. Chen, J.-H., Ozanne, S. E. & Hales, C. N. Methods of cellular senescence induction using oxidative stress. *Methods Mol. Biol. Clifton NJ* **371**, 179–189 (2007).
133. Macleod, K. F. *et al.* p53-dependent and independent expression of p21 during cell growth, differentiation, and DNA damage. *Genes Dev.* **9**, 935–944 (1995).
134. Krenning, L., Feringa, F. M., Shaltiel, I. A., van den Berg, J. & Medema, R. H. Transient Activation of p53 in G2 Phase Is Sufficient to Induce Senescence. *Mol. Cell* **55**, 59–72 (2014).
135. The Size of the Nucleus Increases as Yeast Cells Grow - PMC. https://www.ncbi.nlm.nih.gov/pmc/articles/PMC1951755/.
136. The size-wise nucleus: nuclear volume control in eukaryotes - PMC. https://www.ncbi.nlm.nih.gov/pmc/articles/PMC2080922/.
137. Lanz, M. C. *et al.* Increasing cell size remodels the proteome and promotes senescence. *Mol. Cell* **82**, 3255-3269.e8 (2022).
138. Neurohr, G. E. *et al.* Excessive Cell Growth Causes Cytoplasm Dilution And Contributes to Senescence. *Cell* **176**, 1083-1097.e18 (2019).
139. Cuella-Martin, R. *et al.* 53BP1 Integrates DNA Repair and p53-Dependent Cell Fate Decisions via Distinct Mechanisms. *Mol. Cell* **64**, 51–64 (2016).
140. Ticli, G., Cazzalini, O., Stivala, L. A. & Prosperi, E. Revisiting the Function of p21CDKN1A in DNA Repair: The Influence of Protein Interactions and Stability. *Int. J. Mol. Sci.* **23**, 7058 (2022).

141. Shimi, T. *et al.* The role of nuclear lamin B1 in cell proliferation and senescence. *Genes Dev.* **25**, 2579–2593 (2011).
142. Dou, Z. *et al.* Autophagy mediates degradation of nuclear lamina. *Nature* **527**, 105–109 (2015).
143. Rodier, F. *et al.* Persistent DNA damage signaling triggers senescence-associated inflammatory cytokine secretion. *Nat. Cell Biol.* **11**, 973–979 (2009).